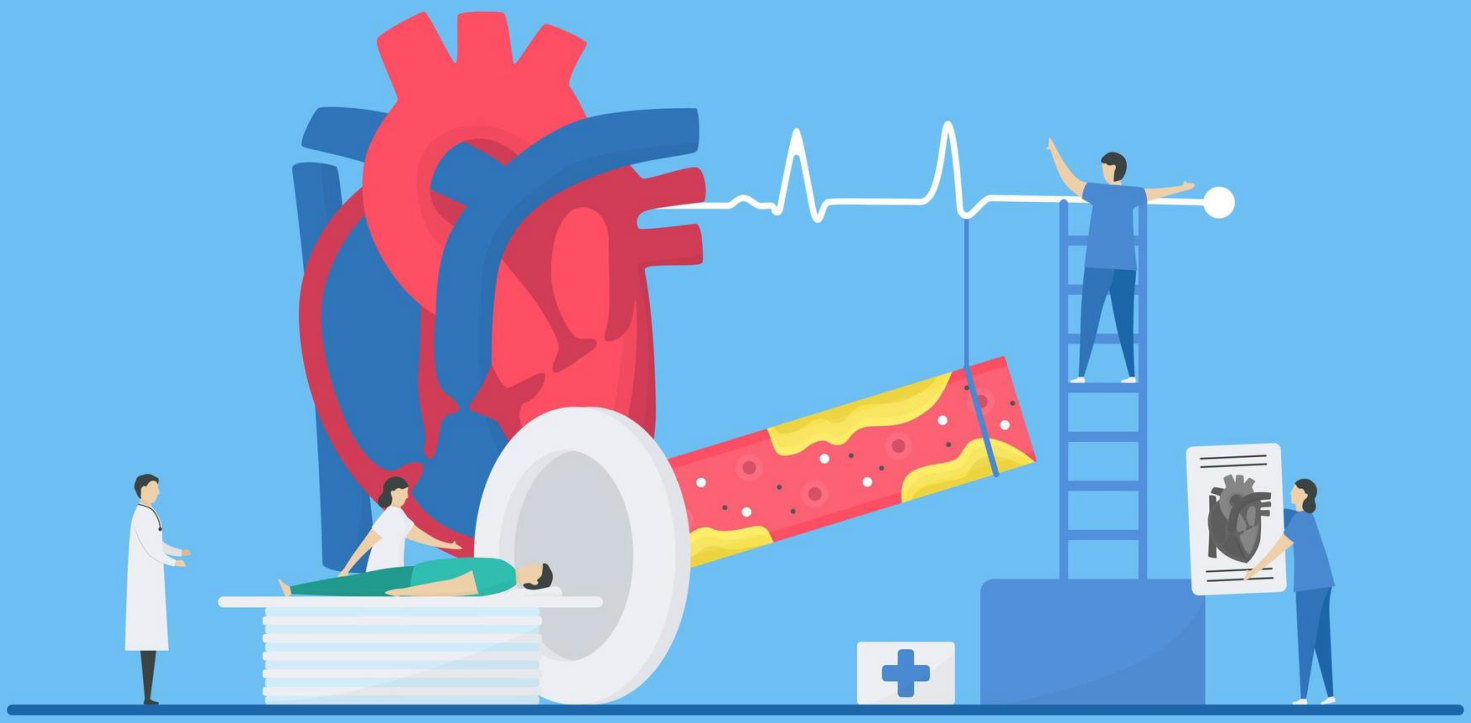

ImPhys - Technische Universiteit Delft

Quantifying myocardial perfusion using 3D magnetic resonance imaging

M. Meskers

TU Delft

Quantifying myocardial perfusion using 3D magnetic resonance imaging

by

Marthe Meskers

to obtain the degree of Master of Science

at the Delft University of Technology,

to be defended on April 30, 2024

Responsible supervisor: dr. S. Weingärtner

Daily supervisor: MSc. A. Arami

Thesis committee: dr. H.J. Vos, dr. M. Menzel

Cover image from Vecteezy

TU Delft Mars Lab

Abstract

Myocardial perfusion, the blood flow to the heart muscle, can be evaluated by tracing the passage of a contrast agent using cardiac magnetic resonance (CMR) imaging. This technique, well-established for diagnosing coronary artery disease, is limited by the necessity for breath-holding, subjective assessment, and low myocardial coverage. In this thesis, we aim to address these limitations of contrast-enhanced myocardial perfusion CMR. We developed a pulse sequence and post-processing pipeline to quantify myocardial perfusion using free-breathing 3D contrast-enhanced CMR. To restrict volume acquisition to the diastolic phase, characterized by minimal cardiac motion, we employed optimal slice oversampling, maximal partial Fourier acquisition, and cartesian undersampling in spatial and temporal domains. To mitigate the effects of breathing, respiratory tracking and image registration were performed. Collaborations for the reconstruction of raw data utilizing deep learning and image registration were established.
Validation in healthy volunteers demonstrates that the developed pulse sequence enables isotropic 3D acquisition (3.6 x 3.6 x 3.6 mm^3) of an arterial input function (AIF) and myocardial signal during each cardiac cycle, up to heart rates of 76 bpm. Obtained AIF images exhibit sufficient resolution for extracting the LV blood pool signal and registered myocardial images are of good quality. We investigated and validated a method to convert signal intensity to T_1, which is required for MBF quantification. While T_1 estimates from the AIF images approximate reference values up to 500 ms well, underestimation was observed from the myocardial images and for high T_1 values.

Contents

1 Introduction

Coronary artery disease (CAD), the obstruction of the arteries responsible for blood flow to the heart muscle (myocardial perfusion), is a leading cause of death worldwide [32]. The evaluation of myocardial perfusion is often necessary to detect ischemia in CAD before patients are referred for cardiac catheterization. Common non-invasive techniques for myocardial perfusion imaging are single-photon emission computed tomography (SPECT), positron emission tomography (PET), and contrast perfusion echocardiography. While SPECT and PET expose patients to ionizing radiation and have a low spatial resolution, echocardiography offers limited myocardial coverage [20]. As an alternative radiation-free technique, cardiac magnetic resonance (CMR) is gaining attention for its high sensitivity and specificity in detecting myocardial ischemia and infarction. Over the last decade, dynamic contrast-enhanced (DCE) CMR has been increasingly used for noninvasive qualitative or semiquantitative assessment of myocardial blood flow and is well established. In this imaging modality, a gadolinium-based contrast agent is injected intravenously. In response, the magnetic resonance signal of well-perfused tissue in the images is enhanced, leaving ischemic regions dark.
Besides the advantages of DCE perfusion CMR compared to other modalities, it is subject to three main limitations. Firstly, the obtained myocardial blood flow maps are mainly assessed visually, giving the diagnoses a subjective nature. Secondly, techniques used to date are constrained by the need for breath-holding of the patient. Lastly, myocardial coverage is low, limiting the confidence by which a coronary stenosis can be correctly identified. The goal of this project is to develop a pulse sequence and establish a post-processing pipeline for quantification of myocardial perfusion using dynamic contrast-enhanced CMR in 3D. With this technique, we aim to improve on each of the mentioned shortcomings of 2D DCE cardiac MR as applied in the clinic. Our approach for each limitation will be explained in more detail below.

Quantification of MBF Currently, highly trained clinicians assess the type and severity of ischemia by visually comparing relative contrast enhancement in DCE myocardial perfusion MR. These diagnoses are therefore subjective and require years of experience in reading myocardial blood flow (MBF) maps. Quantification of MBF using CMR has been proposed to overcome these limitations. Obtained MBF values were shown to obey a linear relationship with PET-derived myocardial perfusion [16] and the technique was proven to have high diagnostic performance for detecting significant CAD [21]. Additionally, quantitative perfusion analysis from high-resolution CMR has higher accuracy in correctly identifying the presence of coronary microvascular dysfunction than visual assessment [37]. Quantification of MBF necessitates an understanding of the gadolinium (Gd) contrast agent concentration in the myocardial tissue. As myocardial contrast enhancement is governed by the arterial input of contrast agent, the arterial input function (AIF) must also be determined. At the high Gd concentrations that are used for perfusion imaging, the relationship between the MR signal and Gd concentration is no longer linear, resulting in a clipped AIF and overestimated myocardial blood flow [26]. To circumvent this, we apply a dual sequence approach, in which a low-resolution image is acquired at the start of the sequence. Subsequently, the myocardial signal will be acquired in high resolution. Once the AIF is known, the MBF can be obtained by application of a tracer kinetics model to the myocardial signal from the high-resolution image and the AIF.

Respiratory motion The passage of contrast agent (approximately 30-50 s) lasts too long for a breath hold [46]. Free-breathing myocardial perfusion CMR is therefore performed, with translational motion of

the heart and possibly motion artifacts as consequence. For visual assessment of perfusion, breathing does not pose a noteworthy problem. For signal extraction in a particular region from a series of images as necessary for quantification, however, techniques to dynamically adjust the field of view along with the respiratory motion and to mitigate motion artifacts are required. In this study, we will employ a respiratory navigation pulse for tracking motion related to breathing. Additionally, in-plane motion will be corrected by image registration, in collaboration with Tao lab.

Myocardial coverage While there is ongoing discussion about the clinical applicability of 3D DCE perfusion imaging when coverage compromises resolution, there is interest in its potential benefits. These include the possibility of increased confidence through acquiring more slices over the same cardiac regions and all slices having been acquired in the same cardiac phase. In current 2D CMR myocardial perfusion examinations, three slices of the myocardium are imaged each cardiac cycle. The slices coincide with the main coronary arteries. To translate from 2D multi-slice to 3D volume acquisition, acceleration is required. In this way, the signal can be sampled during diastole, the quiescent phase of the cardiac cycle. We will reduce the number of profiles of a cartesian sampling pattern by means of spatio-temporal undersampling and partial Fourier acquisition. For reconstruction of the undersampled data with incorporation of coil sensitivity information, a self-supervised deep learning algorithm will be applied, in collaboration with IMAGINE Lab from Minnesota.
Another promising technique for increasing myocardial coverage, which emerged with the introduction of parallel imaging, is simultaneous multislice imaging. In parallel to the development of a quantitative myocardial perfusion sequence in 3D, an initial implementation of simultaneous excitation and acquisition of multiple slices has been attempted, as described in appendix C.

This report is structured as follows. In chapter 2, we introduce the principles of nuclear magnetic resonance and describe the pulse sequence that will be used in this work. Theoretical expressions to relate measured signal intensity to the underlying tissue properties and, ultimately, myocardial blood flow, are explained. We also elaborate on the way cardiac and respiratory motion will be managed during scanning. Next, in chapter 3, the developed perfusion imaging protocol is presented, and the applied acceleration techniques are explained. We describe the experimental method for optimizing scan parameters and for validating the approach for signal intensity conversion. In chapter 4, in vivo scan results and the outcomes of both experiments are presented. Finally, we discuss the obtained results and directions for future research in chapter 5 and give our conclusions in chapter 6.

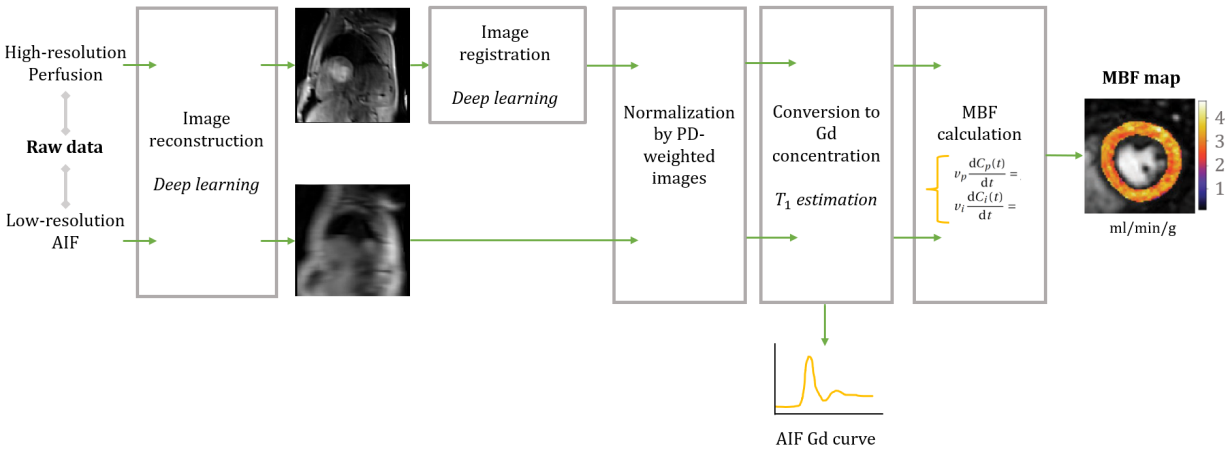

Figure 1.1: Overview of the procedure to obtain a myocardial blood flow map. The method corresponding to a particular step is indicated in italics. Myocardial blood flow map obtained from [40].

2

Theoretical background

In this chapter, the theoretical background necessary to understand the way perfusion maps can be obtained using nuclear magnetic resonance with exogenous contrast enhancement is discussed. We start from the principles of nuclear magnetism and relaxation, describe how the magnetic signal is localized, and then focus on the pulse sequence that will be used. In addition, a brief overview is given of available cardiac imaging modalities for myocardial perfusion assessment and finally, first-pass perfusion imaging is described.

2.1. Nuclear magnetism

The received signal in magnetic resonance imaging (MRI) originates from the magnetic moments of nuclei in the imaging object. Atomic nuclei are positively charged and can be compared to spinning tops if their angular momentum is nonzero. This is the case for nuclei with either an odd atomic number or an odd mass number [34]. The ^1H nucleus has a mass number and atomic number of 1 and is the focus of human MR imaging. Since circulating charge induces a magnetic field, nuclei with angular momentum have a magnetic moment μ oriented along the direction of their spin. This is visualized in Figure 2.1(a). The spin angular momentum is quantized and characterized by the spin quantum number s. This number takes on nonnegative multiples of $\frac{1}{2}$. When nuclei with magnetic moments are placed in a magnetic field $\mathbf{B}$, an energy gap between nuclei with differently oriented magnetic moments arises, known as the Zeeman effect (see Figure 2.1(b)). Most nuclei will occupy the favorable lowest energy state. When summing all individual magnetic moments, the system is found to have a net magnetization $\mathbf{M}(t)$, along the direction of $\mathbf{B}$.

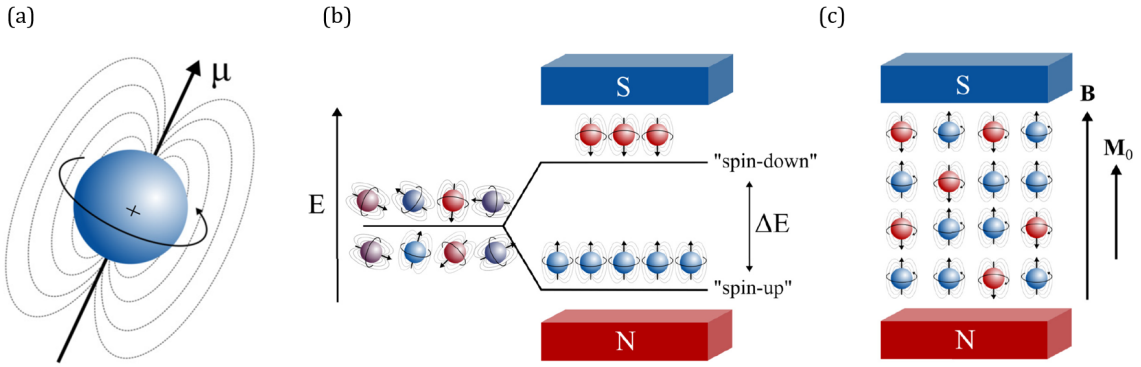

Figure 2.1: a) Atomic nucleus with spin angular momentum and consequent magnetic moment μ. b) The presence of a magnetic field creates a difference in energy between different spin states. c) A net magnetization arises because the spin-up state is energetically more favourable than the spin-down state. Figures adapted from [45].

In presence of an external magnetic field, a magnetic moment experiences a torque, resulting in the following change of cumulative angular momentum $\mathbf{L}(t)$ of the sample

$$\frac{\mathrm{d}\mathbf{L}(t)}{\mathrm{d}t} = \mathbf{M(t)} \times \mathbf{B}. \tag{2.1}$$

The net magnetization is related to the angular momentum by multiplication with the gyromagnetic ratio γ, which is equal to 42.58 MHz/T for the ^1H proton.

$$\mathbf{M} = \gamma \mathbf{L} \tag{2.2}$$

From equations 2.1 and 2.2, it can be derived that the magnetization is static when it is parallel to the external field. However, when it is tilted by an angle θ, the magnetization $\mathbf{M}$ precesses around $\mathbf{B}$, with Larmor frequency $\omega_0 = \gamma B$ [34]. So in order to detect a signal from the nuclear spin system, the magnetization should be oriented away from the external field, such that Larmor precession arises and the dynamic magnetic field will induce current in a nearby coil of wire (Faraday induction). A transverse magnetic field $\mathbf{B_1}$, rotating at frequency ω_1, is used for tilting the magnetization. As transfer of energy is only possible when this magnetic field and the rotating magnetic moments are in resonance, $\omega_1 = \omega_0 = 128$ MHz at 3T. Since the frequency is in the radio spectrum and the magnetic field is applied for a short time interval, it is referred to as an RF pulse. From the origin of the signal in magnetic resonance imaging, we move to the way signal contrast between different tissues is created.

2.2. Relaxation

By applying a secondary magnetic field $\mathbf{B_1}$, energy is added, and the system is brought out of thermal equilibrium. Due to spin interactions, the magnetization will return to its initial state M_0, relaxing back to equilibrium. There are two main relaxation processes that we distinguish: recovery of the magnetization to the initial state parallel to $\mathbf{B_0}$, known as longitudinal relaxation, and the decay to zero of the transverse component of the magnetization, transverse relaxation.
Longitudinal relaxation is a result of energy dissipation of the spin system to surrounding molecules and is, therefore, also called spin-lattice relaxation. The longitudinal magnetization, M_z, recovers in an exponential manner with time constant T_1, which depends on the sample. The recovery following a 90° RF pulse, for example, is described by equation 2.3.

$$M_z(t) = M_0\left(1 - e^{-\frac{t}{T_1}}\right) \tag{2.3}$$

Magnetic moments of nearby nuclei influence the magnetic field that a nucleus in the spin system experiences. For that reason, the effective magnetic field will always be locally inhomogeneous. Moreover, the inhomogeneity varies over time due to molecular motion. The precession frequency of the nuclear spins will start to deviate, reducing the phase coherence in the spin system. The transverse magnetic moments dephase and fan out, such that their superposition M_{xy} decreases to zero. This process is governed by the spin-spin relaxation time T_2:

$$M_{xy}(t) = M_0 e^{-\frac{t}{T_2}} \tag{2.4}$$

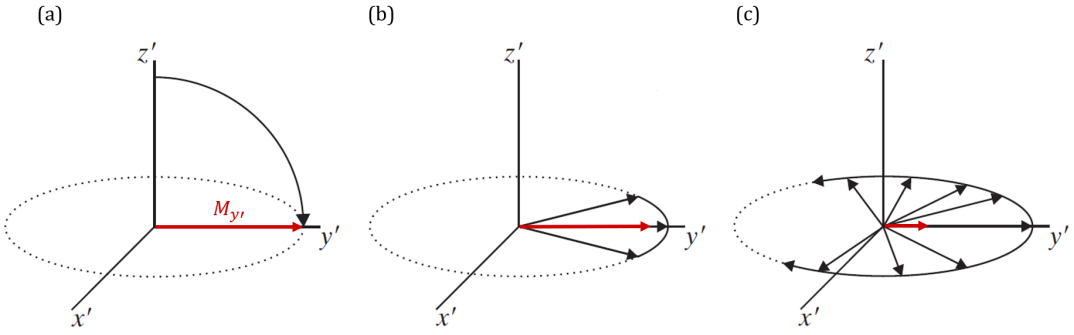

Figure 2.2: Decay of the transverse component of the magnetization $M_{y'}$ in a reference frame rotating around the z-axis with frequency ω_1. After a 90° excitation (a), the magnetic moments fan out in the transverse plane, resulting in a decrease of the net transversal magnetization (b), (c). Adapted from [34].

Phase decoherence of the transverse magnetization is not only caused by spin-spin interactions with time constant T_2. Spatial differences in the strength of the magnetic field contribute to even faster decay. Signal loss due to this type of decay is characterized by time constant T_2' and can be recovered by applying a refocusing pulse to reverse dephasing. Namely, in contrast to the temporally variant field inhomogeneities of T_2 decay, field variations of T_2' decay are static. One cause for these static inhomogeneities is the inevitable inhomogeneity of the main magnetic field. In practice, there is no magnet to obtain an entirely homogeneous field. A second cause is a variation in magnetic susceptibility of different tissues. The constant T_2* combines the reversible T_2 and irreversible T_2' transverse relaxation effects and is given by:

$$\frac{1}{T_2^*} = \frac{1}{T_2} + \frac{1}{T_2'} \tag{2.5}$$

The exponential decay governed by this time constant T_2^* is called free induction decay (FID).

2.3. Spatial encoding

In order to detect a signal from a specific region of the sample instead of only from the superposition of all magnetic moments, the magnetization should be made spatially dependent. This can be accomplished by using magnetic fields which vary linearly in strength along a spatial dimension. The location can, in this way, be encoded in two properties of the magnetic moment: the precession frequency and the phase. Frequency encoding is used for slice selection as well as for reading out samples. The different encoding types and the axes they will be associated with in this study are displayed in Figure 2.3b. Note that for an in vivo scan, the frequency and phase encoding axes may be rotated with respect to the subject, to reduce artifacts. This is further explained in section 3.3.1.

Frequency encoding: The location of a proton can be encoded in its precession frequency by applying a gradient field during sampling. Describing the transverse magnetization at time t and position x as $M_{xy}(x,t) = e^{-i\gamma Bt} M_{xy}(x,0)$, a magnetic field $B(x) = B_0 + xG_x$ will result in the following MRI signal:

$$S(t) = \int e^{-2\pi i\gamma(B_0+xG_x)t} M(x)dx = e^{-i\omega_0 t} \int e^{-2\pi i k_x x} M(x)dx \tag{2.6}$$

After demodulation at the Larmor frequency γB_0, the remaining signal is simply the Fourier transform of the magnetization $M(x)$ with spatial frequencies $k_x = \gamma G_x t$ [34]. Because of this property, the data collected in MR imaging is said to lie in 'k-space'.

Phase encoding: A gradient field can be applied before sampling such that the proton spins accumulate a phase offset depending on their location. During the application of gradient G_y for duration τ, the accumulated phase shift is given by $\phi = \gamma G_y \tau y$. The gradient amplitude G_y is incremented in a stepwise fashion, such that different phase offsets are obtained.

Slice selection: For 2D or multi-slice imaging, a slice can be specified by means of a frequency-selective RF pulse applied in unison with a gradient field. The gradient field along the desired dimension ensures that the resonance frequency varies while the RF pulse excites only the frequency band of the sample that is in resonance. The frequency band thus determines the selected slice, as shown in Figure 2.3a. For 3D MR imaging, phase encoding is used for the third dimension. The magnetization within a volume is excited and sampled, after which images of a number of slices are extracted.

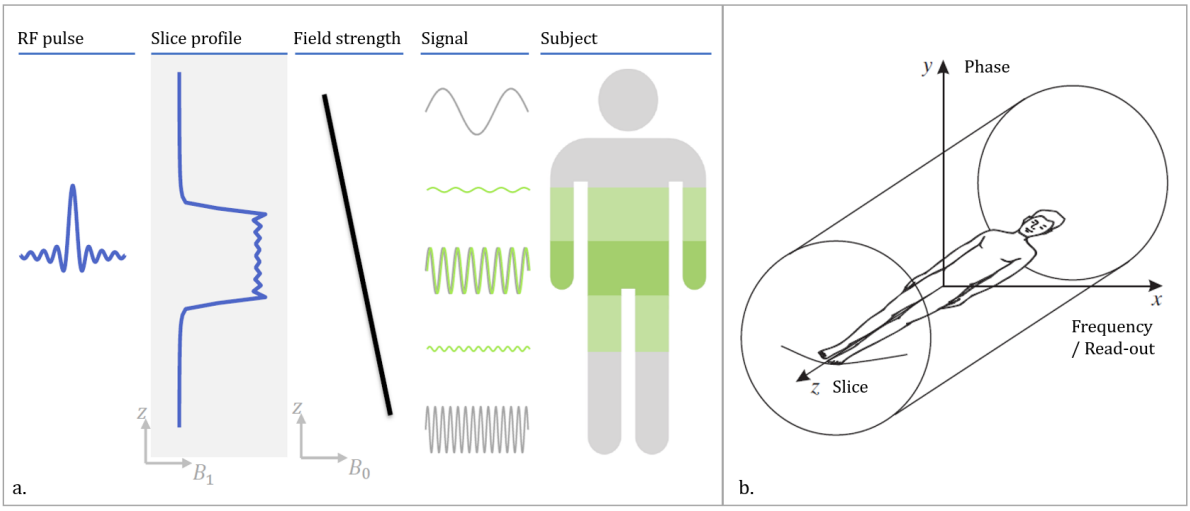

Figure 2.3: a) Schematic overview of slice selective excitation, adapted from [49]. b) Laboratory coordinates and the corresponding spatial encoding method, adapted from [34]

A more detailed description of spatial encoding is given in for example [45]. The fact that the MRI signal is the Fourier transform of the transverse magnetization means that the field of view of the MR image is determined by the sampling distance in k-space: $FOV_i = \frac{1}{\Delta k_i}$, $i = x, y, z$. Turning it around, the desired image resolution determines the maximum number of k-space samples: $\Delta r = \frac{1}{2k_{r,max}}$, $r = x, y, z$.

From the way the detected signal can be connected to the location of the spinning protons it was induced by and the fact that the signal corresponds to a Fourier space, we now turn to the sequences of gradients that enable traversing this space.

2.4. Pulse sequences

An example of a pulse sequence, showing the RF excitation and gradient fields used for spatial encoding, is given in Figure 2.4. Different pulse sequences have been developed for efficient imaging with a high signal for different applications. Pulse sequences can be grouped into two types: spin echo (SE) and gradient echo (GRE) sequences. In SE sequences, the transverse magnetization is retained, while in GRE sequences, the longitudinal magnetization is preserved. Gradient echo sequences are well suited for imaging parts of the body that undergo quick movement because of the property to achieve a short repetition time. In this research, spoiled gradient echo sequences are, therefore, employed for 3D cardiac imaging.

2.4.1. Spoiled gradient echo sequences

RF pulses that tilt the magnetization by a flip angle θ are applied at an interval TR, the repetition time. After each pulse, the magnetization undergoes free induction decay in the transverse plane. Next to this, T_1 relaxation causes the longitudinal component to rebuild. As a result, a steady state longitudinal magnetization is reached after several repetitions [23, 45]. By the use of a small flip angle, the duration of longitudinal relaxation to equilibrium is reduced. Therefore, a short repetition time is feasible, making GRE a fast imaging method.

In the frequency encoding direction, the transverse components of the magnetic moments are first dephased, after which the gradient is inverted to induce rephasing for signal acquisition (see Figure 2.4). As the TR is insufficient for this transverse magnetization to fully decay, a spoiling gradient will be applied to dephase the transverse magnetization at the end of each repetition. Alternatively, eliminating coherent transverse magnetization can be done by randomly varying the RF phase, creating a different direction of the $\mathbf{B_1}$ field for each repetition [53]. This spoiling method is applied in the pulse sequence of this project. Assuming the magnetization has reached this steady state and gets spoiled perfectly after each TR, the signal of a spoiled gradient echo sequence is equal to [13]:

$$S = \Lambda M_0 \left(\frac{sin(\theta)\left(1 - e^{-TR/T_1}\right)}{1 - cos(\theta)e^{-TR/T_1}} \right) e^{-TE/T_2^*} \tag{2.7}$$

In this equation, the scaling factor Λ accounts for the proton density and the receiver coil inhomogeneity. Because the signal is created by the transverse component of the magnetization, the $sin(\theta)$ term appears. The factor e^{-TE/T_2^*} corresponds to the free induction decay following RF excitation. From equation 2.7, it can be derived that increasing θ and reducing TR result in more T_1 weighting. On the other hand, using a small flip angle causes the fraction to converge to $sin(\theta)$ and increases proton density and T_2^* weighting. The influence of T_2^* can be kept minimal by using a short TE.

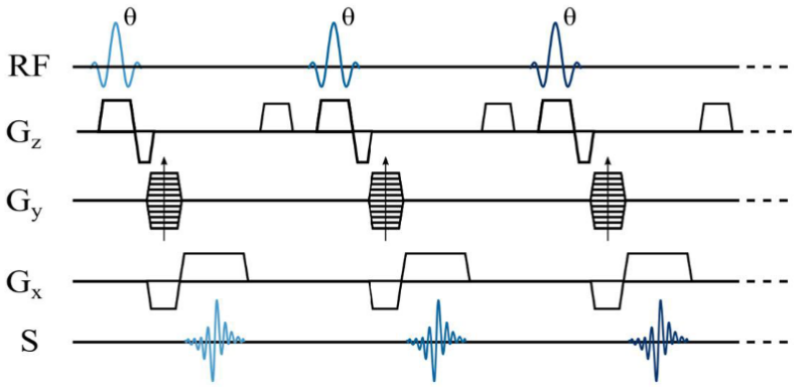

Figure 2.4: Overview of a spoiled gradient echo sequence. From top to bottom the radio frequency pulses, slice encoding gradients, phase encoding gradients, and the read-out gradients are shown. The signal is indicated below. In the z-direction slice encoding gradients and a spoiling gradient at the end of each cycle are applied. The arrow in the phase encoding gradient indicates the stepwise incrementing amplitude to sample all spatial frequencies. Figure from [45].

Spoiled gradient echo sequences are commonly used in myocardial perfusion imaging, which is the topic of this research. We first introduce and compare different available techniques before describing quantitative contrast-enhanced perfusion imaging using CMR.

2.5. Myocardial perfusion imaging

Different diagnostic techniques are currently available in the clinic for assessing myocardial perfusion and detecting ischemia, as already briefly mentioned in the introduction. A common factor in all modalities for myocardial perfusion imaging is that a physical stress condition is created. Specifically, not every coronary stenosis limits the flow of blood to the myocardium at rest. A stress condition can be achieved by physical exercise, but more commonly, a pharmacological vasodilator agent, such as adenosine or regadenoson, is used. In response, the blood vessels widen, increasing the coronary blood flow and mimicking the effect of physical exercise on the heart.

Two widely used methods for myocardial perfusion imaging are single photon emission computed tomography (SPECT) and positron emission spectroscopy (PET), in which gamma, respectively annihilation photons, are detected, originating from a radiotracer in the bloodstream [14]. PET has higher specificity and sensitivity for the detection of coronary artery disease and a higher image quality than SPECT, while SPECT is more widely available and cheaper [35, 43, 50]. Both methods, however, have a relatively low effective spatial resolution: 6-10 mm for PET and 10-14 mm for SPECT [2].

Narrowing or blocking of coronary arteries can also be detected by computed tomography (CT) angiography, where an iodine-based contrast agent is injected to make blood vessels visible on X-ray images. Coronary angiography involves the same principle but includes the insertion of a catheter into a peripheral artery. This allows for localized application of the contrast agent, making it a much more sensitive method than CT angiography, while allowing for immediate intervention after detection of a significant blockage [15]. As this is an invasive technique, it is usually only applied after a non-invasive examination or when immediate intervention is required.

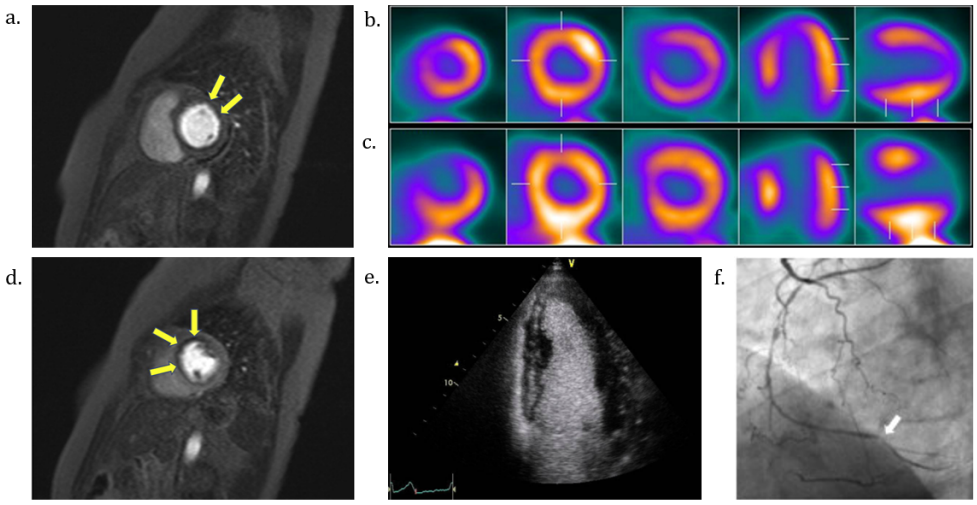

Figure 2.5: Short-axis first-pass perfusion CMR images (basal in a., mid ventricular in d.) during adenosine stress, from [35]. A perfusion defect in the anterior wall of the myocardium is indicated by yellow arrows. Rb-82 PET perfusion images at rest (b.) and during adenosine stress (c.) of the same patient as shown in subfigures a. and d. [35]. Contrast echocardiogram in apical four chamber view (e.) at the end of systole in a patient with recent myocardial infarction referred for assessment of LV systolic function, from [42]. Coronary angiogram (f.) in a patient with a history of coronary artery disease and multiple stents, obtained from [41].

All of the mentioned methods, SPECT, PET, and X-ray angiography, expose the patient to ionizing radiation, which is not the case when using magnetic resonance (MR) or contrast echocardiography for myocardial perfusion imaging. In contrast echocardiography, gas-filled microbubbles are infused intravenously. The replenishment of microbubbles, after they have been destroyed by high energy ultrasound, enables measurement of the blood cell velocity and blood volume fraction [27]. Echocardiography is especially suitable for fast detection of LV contraction abnormalities [22]. The technique, however, is limited by difficult acoustic windows for particular patients and low myocardial coverage [20].

Dynamic contrast-enhanced CMR achieves a higher myocardial coverage than echocardiography and a higher spatial resolution than SPECT or PET for myocardial perfusion imaging [50]. In a perfusion MR scan, two types of contrast between tissue and blood can be used: endogenous contrast, such as arterial spin la-

belling (ASL) or exogenous contrast, as in first-pass perfusion imaging (FPP), where gadolinium-based contrast agents are used. Magnetically labeled blood provides the contrast in ASL, making it especially useful for patients who cannot excrete gadolinium due to kidney failure for example [33]. ASL has already been well established for quantifying cerebral blood flow, but its application to cardiac imaging is still limited due to a low signal-to-noise ratio [3].
In first-pass perfusion imaging, contrast is obtained by administering a solution of a gadolinium compound or an organic gadolinium complex intravenously. Gadolinium (Gd) ions are paramagnetic and locally alter the magnetic field, increasing the spin relaxation rate of hydrogen protons in their surroundings [5]. A difference in T_1 time between blood and tissue is, thus, created by the Gd contrast agent. In the next section, first-pass perfusion imaging and the main challenges for its application to blood flow quantification will be discussed further.

2.6. Quantitative first-pass perfusion imaging

Quantification of myocardial blood flow (MBF) using FPP requires measurement of the Gd concentration over time in the myocardial tissue as well as measurement of the arterial input function (AIF). This function describes the delivery of contrast agent and is commonly obtained by extracting the Gd concentration from the left ventricular blood pool. To determine the [Gd]-time curve from a direct conversion of the MR signal, the signal would have to be directly proportional to [Gd]. This holds for low concentrations. At high gadolinium concentrations, as seen in the blood pool, however, saturation of the signal intensity takes place, and the relationship is not linear anymore [7]. This happens because gadolinium does not only shorten T_1, but T_2^* as well. Signal enhancement is observed up until a certain concentration, depending on the tissue and pulse sequence parameters. For higher concentrations, T_2^* decay dominates, and the signal decreases (see Figure 2.6a). As a result, the arterial input function will be saturated, as illustrated by Figure 2.6b.

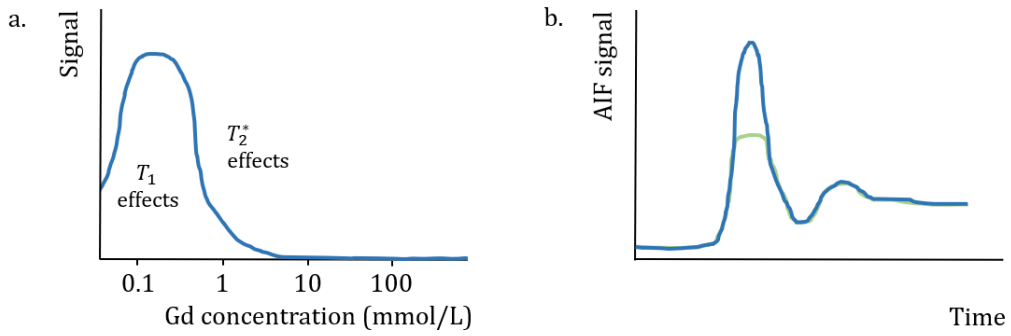

Figure 2.6: a. Effect of gadolinium concentration on signal intensity, adapted from [9]. b. True (blue) and clipped (green) arterial input function.

To correct for AIF saturation, two methods can be applied: the dual bolus or the dual sequence method.
In the dual bolus approach, diluted contrast agent is first injected, before the main bolus of non-diluted contrast agent (with the same volume and flow rate) gets injected [38]. The pre-bolus image can be used to correct for the non-linearity of the signal-[Gd] relation. In the other approach, dual sequence, two different images are acquired after only a single injection of contrast agent. Because this makes the clinical workflow simpler compared to the dual bolus method, it is more widely applied. As the aim of this project is to develop a clinically applicable method for quantifying MBF with high coverage using FPP imaging, the dual sequence approach is used.
At the start of the sequence, a low-resolution image is acquired with short acquisition time for determination of the AIF. In this way, T_2^* dephasing and consequent saturation of the signal intensity is minimized. Subsequently, the myocardial signal is acquired in high resolution. These two acquisitions will be referred to as imaging stacks from now on, following the nomenclature of the way they are programmed.
A myocardial blood flow map in units of mL/min/g can be obtained by means of a myocardial tissue model, such as Fermi constrained deconvolution or a distributed parameter model [51]. This, however, first requires conversion of the AIF and myocardial signal to units of gadolinium concentration (mmol/L).

2.6.1. Signal intensity-to-[Gd] conversion

Using the relaxivity r_1[L/mmol-s] of the used contrast agent, T_1 and $T_{1,0}$, the spin-lattice relaxation time with and without contrast agent, the Gd concentration can be computed [7] [26]:

$$\frac{1}{T_1} = \frac{1}{T_{1,0}} + r_1 \cdot [Gd] \tag{2.8}$$

This means that the T_1 value must be determined at each moment. T_1 maps are usually obtained by monitoring the recovery of the magnetization after an inversion or saturation pulse. Equation 2.3 is then fitted to the signal intensity vs. time curve to obtain T_1. Since acquisition time is scarce for cardiac perfusion imaging and especially for 3D imaging, T_1 will be determined via a single-point measurement in combination with Bloch signal calculations instead. We use the method as presented by A. Cernicanu and L. Axel in [7]. In this method, the magnetization under influence of the saturation and excitation pulses is calculated by applying the longitudinal magnetization solution of the Bloch equation repeatedly. By taking the magnitude of the transverse magnetization at the moment when the center of k-space is acquired as the effective signal, a closed-form expression of the signal intensity as a function of T_1 and relevant imaging parameters was derived [7]:

$$\begin{aligned} S(T_1, TR, TD, \alpha_{T_1}, \alpha_{PD}, n) &= \frac{S_{T_1}}{S_{PD}} \\ &= \frac{\Lambda M_0 sin(\alpha_{T_1})\Big[(1-e^{-TD/T_1})\cdot\left(e^{-TR/T_1}cos(\alpha_{T_1})\right)^{n-1} + \left(1-e^{-TR/T_1}\right)\cdot g(\alpha_{T_1})\Big]}{\Lambda M_0 sin(\alpha_{PD})\Big[\left(e^{-TR/T_1}cos(\alpha_{PD})\right)^{n-1} + \left(1-e^{-TR/T_1}\right)\cdot g(\alpha_{PD})\Big]} \end{aligned} \tag{2.9}$$

in which the function g is given by:

$$g(\alpha) = \frac{1-\left(e^{-TR/T_1}cos(\alpha)\right)^{n-1}}{1-e^{-TR/T_1}cos(\alpha)}. \tag{2.10}$$

The parameters TR and TD correspond to the repetition time and the delay time between saturation and the start of acquisition. The T_1-weighted image is normalized by a proton density-weighted image, such that the variation in proton density, inhomogeneity of the receiver coils (indicated by Λ), and the initial magnetization M_0 are not of influence anymore. For the PD-weighted image, a flip angle of α_{PD} and no 90° saturation prepulse are used, while the T_1-weighted image is obtained after a saturation pulse and RF pulses with flip angle α_{T_1}. The parameter n indicates the number of imaging RF pulses of this angle that are applied before the acquisition of the center of k-space.

2.7. Blood-tissue exchange model

The next step in the workflow towards an MBF map encompasses the modelling of tracer kinetics between blood and tissue. Such a blood-tissue exchange (BTEX) model was not yet applied to dynamically contrast-enhanced 3D perfusion scans in this project, as in vivo scans with enhanced contrast were not acquired. For a complete understanding of the steps that lead to a quantitative myocardial blood flow map, however, we briefly explain the theory of BTEX models.

A perfusion unit (for example a single voxel) is usually modelled as a system of two interacting compartments: the plasma and the interstitium, the space between blood vessels and cells [39]. The model consists of two coupled differential equations that describe the evolution of tracer concentration as a non-linear function of physiological parameters, for example, MBF. Several models have been proposed in the past years with varying complexity and physiological interpretation. Fermi-constrained deconvolution as proposed by Jerosch-Herald et al. [25] allows calculation of MBF but does not involve other kinetic parameters and is not physiologically motivated. Scannell et al. [39] use the following two-compartment exchange model for the evolution of the tracer concentration in plasma $C_p(t)$ and interstitial space $C_i(t)$:

$$v_p \frac{\mathrm{d}C_p(t)}{\mathrm{d}t} = F_p \cdot \big(C_{AIF}(t) - C_p(t)\big) + PS \cdot \big(C_i(t) - C_p(t)\big) \tag{2.11}$$

$$v_i \frac{\mathrm{d}C_i(t)}{\mathrm{d}t} = PS \cdot \big(C_p(t) - C_i(t)\big) \tag{2.12}$$

In 2.11 and 2.12, C_{AIF} indicates the AIF concentration, v_p and v_i the fractional interstitial and fractional plasma volume and PS the permeability-surface area product. Hct denotes the hematocrit value which is used to convert the plasma blood flow F_p to MBF, indicated by F_b: $F_b = \frac{F_p}{1-Hct}$. Also the blood [Gd] was converted to plasma concentration using the hematocrit value: $C_p(t) = \frac{C_b(t)}{1-Hct}$. The gadolinium concentration in tissue observed in the MR image is the sum of the plasma and interstitial concentrations:

$$C(t) = v_i C_i(t) + v_p C_p(t). \tag{2.13}$$

Hue et al. proposed a BTEX model which includes the influence of Gd extracted from the vascular space into the interstitial space. This approach makes the differential equations spatially dependent and adds terms $v_p D_p \frac{\mathrm{d}^2 C_p}{\mathrm{d}x^2}$ and $v_i D_i \frac{\mathrm{d}^2 C_i}{\mathrm{d}x^2}$ to equations 2.11 and 2.12 respectively. D_p and D_i are the molecular diffusion coefficients within the plasma and interstitium. Equations 2.11 and 2.12 can be solved analytically by using the Laplace transform. The model by Hue et al., however, is solved by means of a finite element method.

2.8. Motion management for quantitative cardiac MR

Motion of the heart between images of different heartbeats is undesired for normalization of the images by the PD-weighted image acquired in the first cardiac cycles. For obtaining a series of cardiac images without deformation and translation of the heart, cardiac motion and motion due to respiration need to be taken into account. In this section, cardiac synchronization and respiratory navigation, techniques to diminish the effect of both sources of motion, will be discussed.

2.8.1. Cardiac synchronization

In cardiac MR, data is ideally collected during diastole of both chambers, when the atria and ventricles are relaxed and motion is minimal. Figure 2.7 shows the cardiac cycle with its different phases. The acquisition must be synchronized with the cardiac cycle, for which Electrocardiogram (ECG) prospective triggering is generally used. The R-peak of the cardiac cycle is detected and followed by a trigger delay. This delay defines the time between the R-peak and excitation of k_0, the center of k-space. In this way, it will always be sampled during the same moment within the cardiac cycle, giving images from different cycles the same contrast.

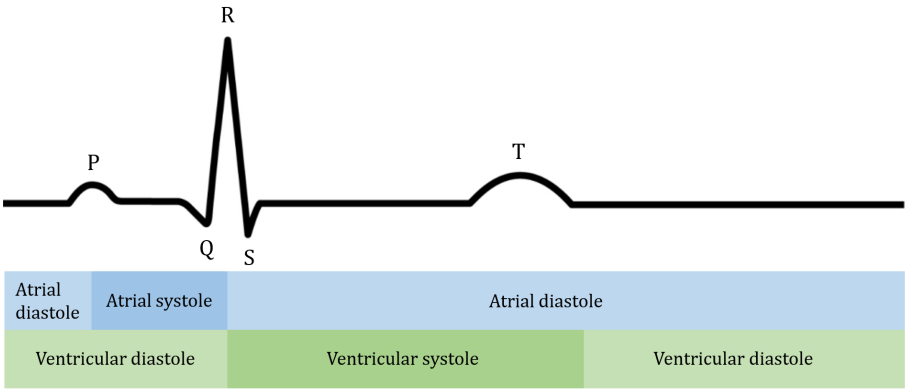

Figure 2.7: Connection between the cardiac cycle and an ECG. The R-peak, as well as the phases of contraction and relaxation (systole and diastole, respectively) of the atria and ventricles are indicated. For a detailed description of the cardiac cycle, the reader is referred to [8].

2.8.2. Respiratory navigation

In a clinical myocardial perfusion study, the heart of a patient will be imaged for 60-90 heartbeats, to fully cover the first passage of contrast agent. Because this is too long for a breath hold, the patient breathes freely. The consequence is that the position of the heart is variable, and motion artifacts may arise. In free-breathing MR imaging, feet-head motion related to respiration can be monitored with a respiratory navigator. This is a selective RF pulse applied to a rectangle or cylinder within the body, usually centered around the dome of the liver. The echo of the pulse allows to image the movement of the diaphragm and, by means of an empirical conversion, deduce the motion of the heart. A respiratory navigator pulse can be leading or trailing with respect to the image acquisition. When using both a leading and trailing navigator, acquisitions after which the diaphragm did not return to its initial position, and therefore correspond to inspiration, can be discarded. These acquisitions will be repeated, until they are synchronized with expiration. This technique, called respiratory gating, thus prolongs the scanning duration. In this project, we made use of respiratory tracking, which involves only a leading navigator. The position of the object of interest is determined just before image acquisition, and in real-time, the imaging window is adjusted to this position. The anatomy of interest, the heart in this case, will, therefore, remain in approximately the same position within the window. For perfusion imaging, it is not possible to use respiratory gating in addition to tracking since an image of each heartbeat is required to accurately trace the bolus passage with sufficient temporal resolution.

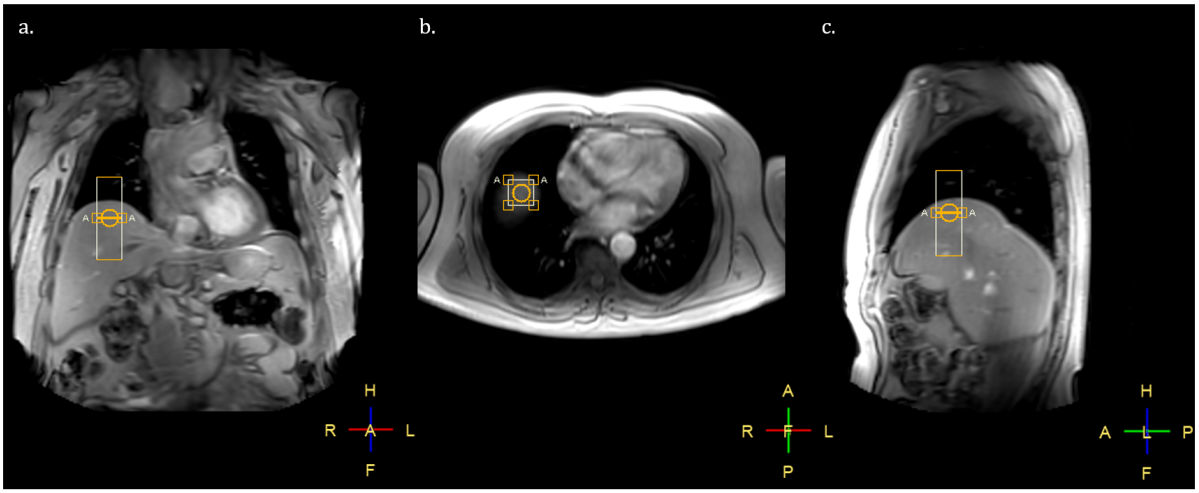

Figure 2.8: Positioning of the respiratory navigator around the dome of the liver, shown in coronal (head to foot, a.), transverse (right to left, b.) and sagittal (anterior to posterior, c.) orientation.

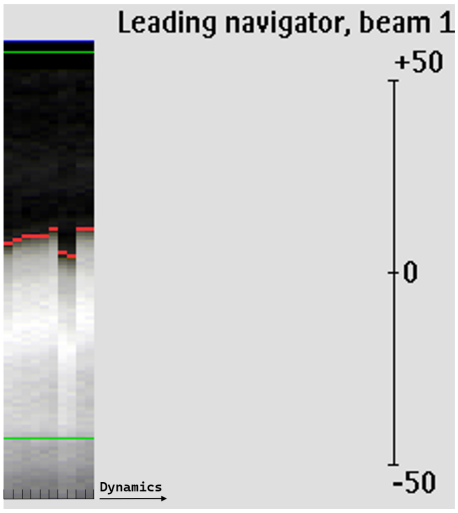

Figure 2.9: The navigator window of an in-vivo scan comprising 10 dynamics. The scale bar indicates the displacement in mm, and the red line is the detected tissue boundary.

3

Method

In this chapter, we present the developed pulse sequence and selected scan parameters for 3D quantitative FPP imaging. In order to image a volume enclosing the heart during diastole, an accelerated acquisition is required. We describe the techniques that will be used to achieve sufficient acceleration as well as an experiment to determine the minimal feasible oversampling rate. Finally, the implementation of single-point T_1 measurement and a validation experiment in phantom are discussed.

3.1. Pulse sequence

A schematic overview of a dual sequence myocardial perfusion scanning procedure is given in Figure 3.1. First, A proton density-weighted (PD) scans of the heart will be acquired before contrast agent injection. The differences between PD-weighted and T1-weighted scans are the lack of a saturation pulse for the PD-weighted image and the lowering of the flip angle to 4° to decrease T_1 weighting, as can be derived from equation 2.7. Following administration of the contrast agent bolus, the heart will be imaged each R-R interval for the duration of the bolus passage. This takes 1 to 2 minutes, depending on the heart rate of the patient. The PD and T1-weighted images are acquired in the same examination, which automatically enables the saturation pulse and increases the excitation flip angle after A dynamics.

During each R-R interval, first the longitudinal magnetization is prepared to a zero state by a non-selective composite saturation RF pulse. The acquisition of both imaging stacks is performed instantaneously after application of this composite pulse. The shortest possible saturation time (TS), between saturation and acquisition of the center of k-space, k_0, was selected in order to reduce the sequence duration. On the other hand, the trigger delay, the time between the R-peak and excitation of k_0, was given the longest possible value. In this way, the acquisition is synchronized with the diastolic phase.
The protocol parameters of the scanning sequence are listed in table 3.1. Table 3.2 contains the parameters that apply to stack 1 for AIF imaging in particular and differ from the main imaging stack. After the magnetization is prepared by the saturation pulse, a low resolution image is acquired for extraction of the arterial input function. To achieve this, the k-space as shown in figure 3.3 is restricted to a rectangle of 9 k_y by 7 k_z samples, centered around k_0. The read-out sampling is unaffected. The highest sampled spatial frequencies in phase and slice direction are therefore $k_{y,max} = 4 \cdot \Delta k_y = \frac{4}{FOV_y} = \frac{4}{302}$ mm^{-1} = 0.133 cm^{-1} and $k_{z,max} = \frac{3}{FOV_z} = \frac{3}{300}$ mm^{-1} = 0.1 cm^{-1}. For the number of samples, minimum values that still permit distinction of the left ventricle have been selected. The pulse sequence is programmed in such a way that the sampling range for k_y and k_z can be easily changed before performing a scan. In practice, frequency encoding is performed during dead time within a repetition, while each phase encoding step requires additional repetitions. A reduction in k_y and k_z profiles, therefore, lowers the acquisition time, as opposed to a reduction of k_x measurements.

After acquisition of the low-resolution images, the respiratory navigator pulse is played, the signal received, and the scanning window adjusted before the magnetization is again saturated. After this second preparation, the magnetization signal will be sampled according to the trajectory shown in figure 3.3 and described in section 3.2.1.

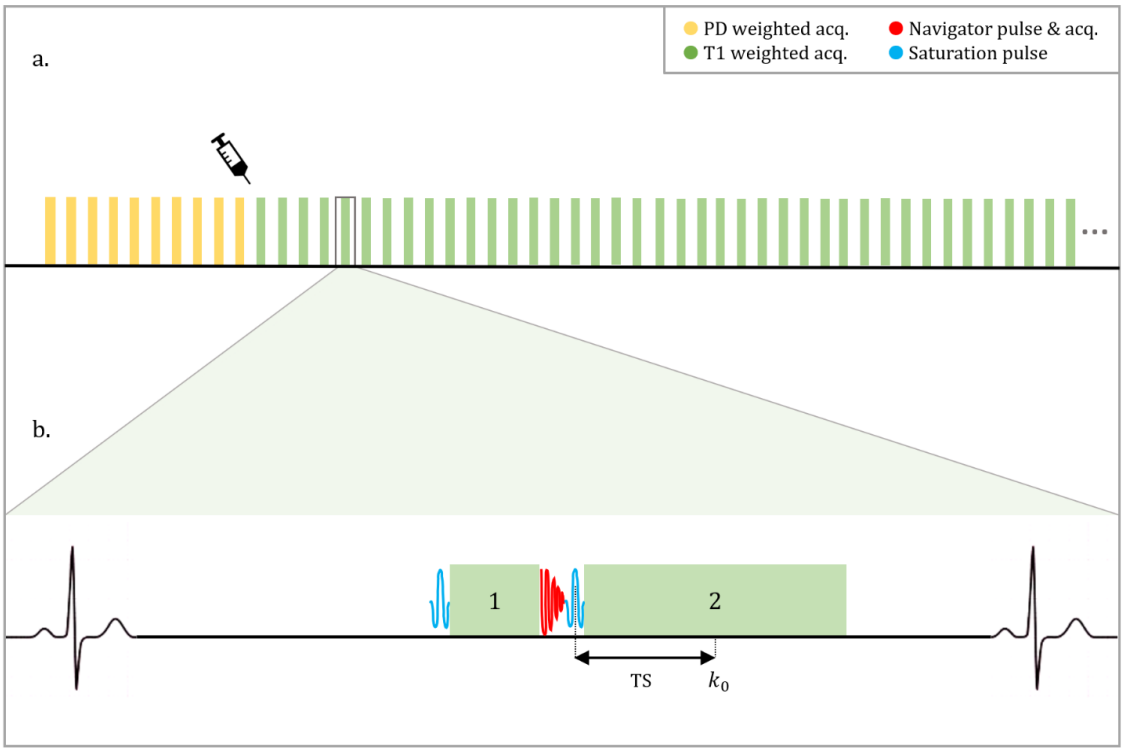

Figure 3.1: Schematic overview of the applied myocardial perfusion imaging pulse sequence. Subfigure a. shows the acquisition of 10 proton density-weighted images, the injection of contrast agent, and the repeated acquisition of T1-weighted images. Subfigure b. indicates the components of the sequence within each cardiac cycle: the respiratory navigator pulse, the saturation pulse, the acquisition of a low-resolution image for AIF extraction, and the acquisition of high-resolution images for the myocardial signal.

The orientation and field of view of the scans were determined in consultation with a radiologist. A common orientation in cardiac MRI is the short-axis (SAX) view, which is perpendicular to the long axis of the heart (indicated in figure 3.2) and shows the right and left ventricles. This orientation will be used for the 3D myocardial perfusion scans of this project. In long-axis direction, 102 mm is a sufficient FOV in order to fully cover the myocardium from base to apex throughout the cardiac cycle, for most subjects. As a reference, a healthy volunteer scan of the heart in a 2-chamber view is shown in figure 3.2. This image was acquired in end-diastole, when the distance between apex and base of the heart is the largest. The in-plane FOV of 300 x 302 mm^2 is large compared to the heart in order to reduce fold-over artifacts, which will be described in more detail in section 3.3.1.

The duration of the total sequence, comprising preparation, navigation, and imaging of both stacks, is equal to 539.8 ms. This is achieved by strongly accelerating the acquisition, as will be described in the next section. An isotropic resolution (almost equal voxel sizes in all directions) has been chosen to facilitate the reformatting of the scan to different imaging planes retrospectively.

Respiratory navigation would normally be performed before each imaging stack for multi-stack CMR. The decision and adjustment to the pulse programming code has been made to only track respiration before the second imaging stack, because the images of the first stack are solely meant for extracting the intensity-time curve in the left ventricular blood pool. If a sufficiently large ROI is selected that remains well inside the LV for all the imaged slices, translational motion due to breathing does not pose a problem.

The pulse sequence was tested in vivo on a healthy volunteer. No contrast enhancement scans on patients were performed during this project, as approval from the Medisch-ethische Toetsingscommissie was still pending.

Table 3.1: Protocol parameters for myocardial signal measurement (stack 2) at 3T

K-t acc. factor	10
PD dynamics	10
α_{PD}	4°
TE	0.73 ms
TR	1.90 ms
Bandwidth	3420.9 Hz
α_{T1}	12°
FOV	300 x 302 x 102 mm^3
Matrix size	84 x 85 x 29
Voxel size	3.57 x 3.55 x 3.55 mm^3
Halfscan factors	$h_y = 0.62, h_z = 0.847$
Partial echo factor	0.625
TS / TD	177.0 / 5.74 ms
Exc. pulses before k_0 acq.	91
Imaging duration	366.0 ms

Table 3.2: Protocol parameters for AIF measurement (stack 1) at 3T

k_y sampling range	[-4, 4]
k_z sampling range	[-2, 2]
TS / TD	64.9 / 5.74 ms
Exc. pulses before k_0 acq.	32
Imaging duration	120.0 ms

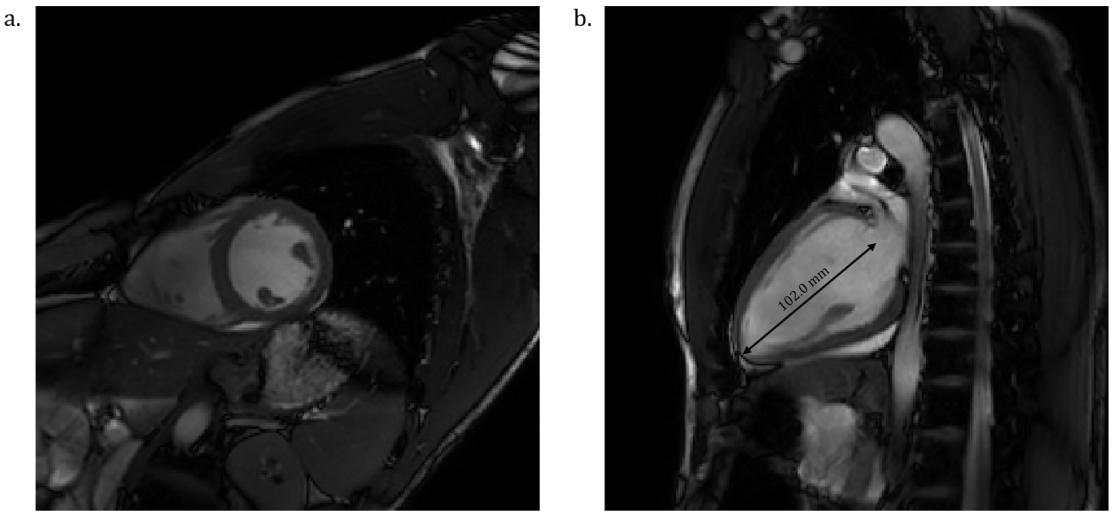

Figure 3.2: Short-axis (a.) and 2-chamber (b.) view of the heart of a healthy volunteer. Both images were acquired in end-diastole, when the heart is at its largest. The length measurement of 102.0 mm along the long axis in b. corresponds to the FOV in slice direction of the 3D perfusion sequence.

3.2. Acceleration techniques

The scanning time can be reduced by using redundancy of the signal in the spatial and temporal domain and additional information from the receiver coils. In sensitivity encoding, abbreviated as SENSE, the sensitivity of the different coils is taken into account when localizing the signal. By including that magnetization at a specific position is best detected by the nearest coils in the reconstruction problem, the number of phase encoding steps can be reduced to still achieve an image of the same resolution. Undersampling is applied to the phase encoding direction as the number of phase encoding steps drives the total scan duration. When also sampling sparsely over multiple repetitions (referred to as dynamics) and thereby taking advantage of temporal correlation of the signal, the sequence can be accelerated even more. Temporal correlations in the signal are typically present when imaging an object undergoing periodic motion, such as the heart or the lungs, and acquiring the signal at a regular time interval. In the method k-t BLAST (Broad-use Linear Acquisition Speed-up Technique), this principle is applied, along with an estimation of the signal intensity in space [47]. Additionally, there is a method that uses both spatiotemporal correlations as well as coil sensitivity, called k-t SENSE. In this project, k-t BLAST acceleration was used. The reconstruction will not be performed in-line by the scanner, but by means of a self-supervised learning algorithm developed by collaborators Mert Acar and Mehmet Akçakaya. This offers the opportunities for employing the coil sensitivity information without storing it, as is the case for k-t SENSE. Namely, the coil sensitivity can be extracted from a k-space window that is fully sampled.

3.2.1. K-t BLAST

The k-t BLAST acceleration technique consists of two cartesian acquisition stages: the undersampled stage and the training stage. In the undersampled stage, the data is sampled with a spacing in phase direction equal to the acceleration factor A. The training stage involves the acquisition of a fully sampled region of low frequencies and is meant for obtaining a low-resolution estimate of the time-varying object. The stages can be performed after each other, where first A undersampled images are acquired during A heartbeats, then a training scan is performed, or the training profiles can be interleaved into the undersampled stage and also acquired each dynamic. Interleaving of the training profiles is recommended for perfusion imaging with a contrast agent, as the imaging contrast varies from dynamic to dynamic.

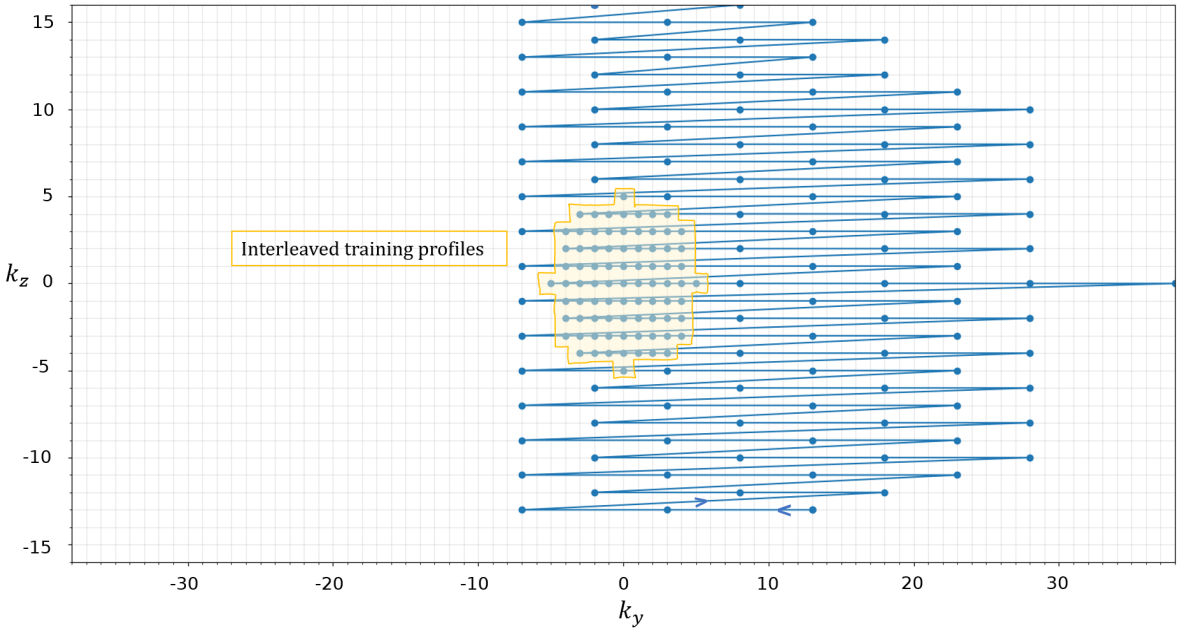

Figure 3.3: Cartesian k-space sampling trajectory of a k-t BLAST factor 10 accelerated scan with halfscan factors $h_y = 0.62$ and $h_z = 0.847$. The start and direction of traversal are indicated with arrows.

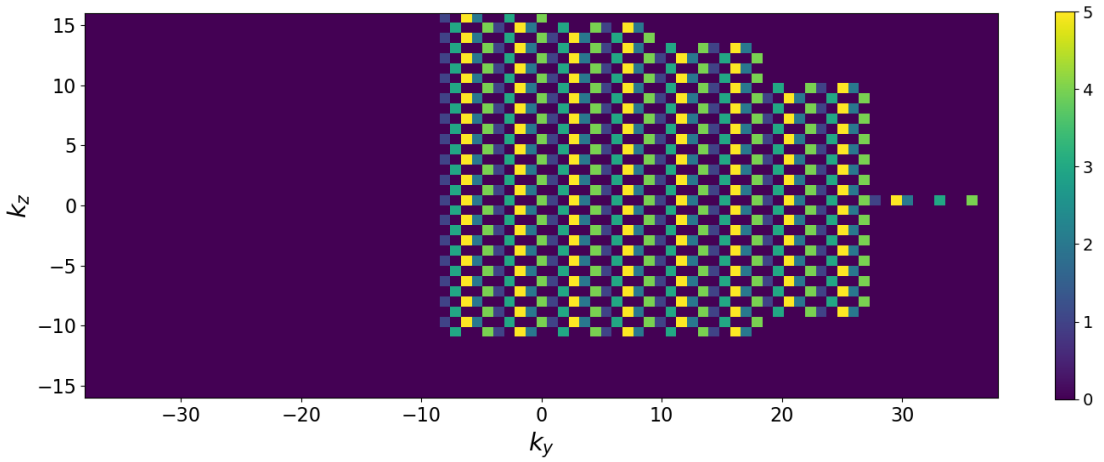

Figure 3.4: K-space sampling patterns of the undersampling stage of the first 5 dynamics of a k-t BLAST scan. Acceleration factor 10 and halfscan factors $h_y = 0.62$ and $h_z = 0.847$ were used. The colourbar indicates the idex of the dynamic, starting from 1.

The maximum number of training profiles in each direction can be selected and for the 3D perfusion sequence, it was set to 11. Figure 3.3 shows the resulting k-space sampling pattern of one dynamic of a scan with k-t BLAST factor 10 acceleration. The interleaved training profiles are delineated, and all other profiles obey a spacing of $A = 10$ in y-direction. Note that the k_y axis is traversed in reverse linear order, linearly from high to low frequencies. This is selected to postpone the acquisition of k_0 such that it coincides with diastole as much as possible for cardiac motion reduction.
The undersampling pattern is shifted each dynamic, such that all spatial frequencies are sampled once after A dynamics, and the low frequencies of the training stage are sampled A times. Figure 3.4 shows sampling patterns of the undersampling stage of 5 from 10 dynamics.

3.2.2. Partial Fourier acquisition

A second acceleration technique finds its origin in the conjugate symmetry of k-space of real-valued objects: the signal at coordinate (k_y, k_z) is the complex conjugate of the signal at $(-k_y, -k_z)$. In theory, it is therefore sufficient to acquire data from one-half of k-space only, if the image was real-valued. In practice, however, phase errors may occur because of for example variations in the B_0 field, the RF transmit phase, or coil sensitivity [11]. Therefore, a minimum of 62.5% of k-space is acquired to extract the phase pattern, before employing the k-space symmetry. While the resolution of the resulting image is unaffected by applying halfscan in the phase or slice encoding direction, the signal-to-noise ratio (SNR) is reduced, depending on the chosen percentage of sampled k-space. Next to the in-plane directions, it is also possible to use conjugate symmetry in the frequency encoding direction. When using this technique, referred to as partial echo, only the final part of each echo is sampled.

3.3. Image registration

Despite the applied respiratory navigation and ECG triggering, there may be misalignment and deformation of the myocardium over the acquired dynamics. By means of retrospective image registration, the heart can be aligned in all images of the same slice, such that the signal of a region of interest (ROI) can be easily extracted and compared over time. Image registration was performed by Yi Zhang using a method based on VoxelMorph, a fast, learning-based framework for deformable image registration. A more detailed description of the registration method can be found in [1] and [44]. The images are registered pairwise to the proton density-weighted image by which they will be normalized. The similarity metric or image matching criterion that was used, is the normalized mutual information, as defined and described in [36].

3.3.1. Oversampling to mitigate fold-over artifacts

When the imaging object extends beyond the field of view of a magnetic resonance scan, signal from outside the FOV can get folded into the image. This is due to aliasing in combination with an imperfect excitation profile. It can occur in all three spatial encoding directions but is most severe in the phase encoding direction.

The profile of the excitation RF pulse is not a pure block pulse with sharp edges, such that some RF power is also delivered outside of the field of view. In the frequency encoding direction, for example, a high frequency from this region may incorrectly be detected as a low frequency if the sampling rate is insufficient. Fold-over in the frequency direction can easily be prevented by taking more MR signal measurements than necessary for the desired FOV. Since this does not increase the acquisition duration, a default oversampling factor of 2 is a common choice for the frequency encoding direction.

The FOV in the other two dimensions in 3D MR imaging is encoded by a phase offset of the precessing magnetic moments. Figure 3.5 shows a field of view that is encoded by phase offsets between 0° and 360°. A higher or lower phase offset of anatomic regions outside this FOV may erroneously get mapped to a phase within this window. Fold-over can be prevented by means of additional sampling beyond the border of the FOV.

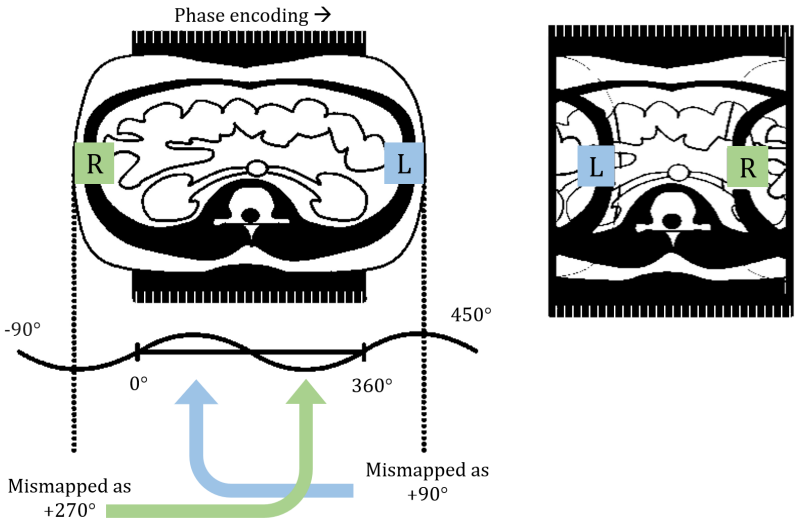

Figure 3.5: Fold-over artifact in phase encoding direction. Adapted from [12]

As additional phase-encoded samples require more repetitions and the duration of the 3D perfusion sequence should not be unnecessarily increased, the smallest FOV that prevents fold-over in phase direction should be used. An experiment was set up to determine the minimum slice oversampling factor for this purpose. A homogeneous phantom bottle was scanned with the developed 3D perfusion sequence and with a slice oversampling factor of 3. This means that the magnetization in 29 slices was excited, and the signal of 3 times as many slices was sampled, as illustrated by figure 3.6. The images of the acquired 87 slices can be obtained by performing an inverse fast Fourier transform to the raw data, as described in section 2.3, and taking the sum of squares of each receiver channel. We use this offline reconstruction because the scanner only reconstructs the FOV, while we are interested in the excitation profile inside as well as outside the FOV. More information on exporting the raw data from the scanner and converting it to a k-space matrix can be found in appendix B. Different excitation pulses have been used to investigate which pulse allows for the lowest slice oversampling.

A region of interest (ROI) of 14 by 13 pixels in the middle of the bottle was selected, as indicated in Figure 3.6b. The average intensity in this region was computed and plotted as a function of slice index.

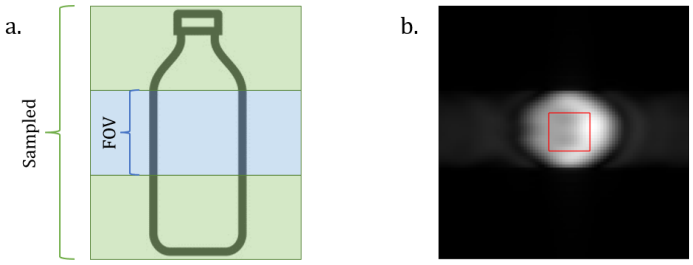

Figure 3.6: a.) Imaging set-up to visualize the slice excitation profile and determine the minimum suitable slice oversampling factor for the 3D perfusion sequence. For the experiment, a slice oversampling factor of 3 was used. b.) Slice 49 of the phantom bottle with the ROI indicated in red, reconstructed offline.

3.4. Single-point T1 measurement for quantification

Relation 2.9 was implemented in Matlab as a subtraction of the measured normalized signal intensity and the equation on the right-hand side. In this way, fzero in Matlab's [29], for finding the root of a nonlinear function, could be used to obtain T_1 estimates.

The T1MES phantom was scanned with the developed 3D perfusion pulse sequence. This phantom has 9 vials with known T_1 and T_2 values that approximate myocardium and blood before and after Gd contrast enhancement, as shown in figure 3.7 [6]. A square with 4 by 4 pixels will be selected in each vial in scanner reconstructions of the PD- and T_1-weighted scans. For the second stack, the PD-weighted intensities will be replaced by the average intensity of the considered square region in order to prevent noise enhancement, as proposed in [7]. The intensity of each of the 16 pixels will be used, taking the scaling of the DICOM images into account, to compute the T_1 estimates. An average T_1 value and standard deviation will then be obtained for each vial.

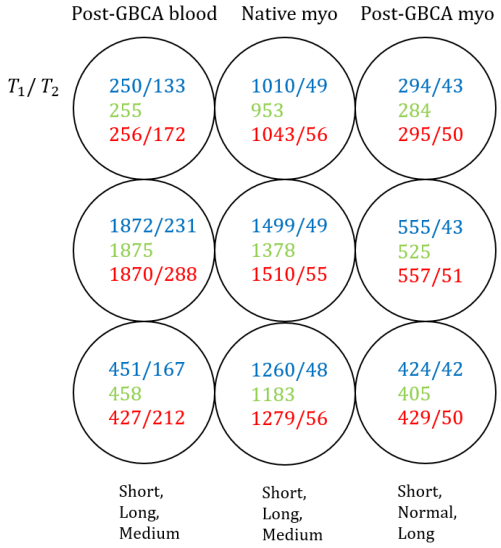

Figure 3.7: T_1 and T_2 values in ms of the T1MES phantom at 3T, from [6]. In blue, slow scan reference data is displayed: slow inversion recovery spin echo for T_1 and slow spin echo for T_2. T_1 values shown in green represent the mean value per vial derived from tests on five model phantoms using a variant of MOLLI adapted for native T_1 mapping. Red values represent the values obtained by the manufacturer in Australia using a 1.4 T Bruker minispec relaxometer at 22 °C. The relaxation times of each column approximate post-gadolinium based contrast agent myocardium, native myocardium and post-contrast blood.

In order to assess the accuracy of the single-point T_1 measurement technique applied to scans with the developed 3D perfusion sequence, the obtained estimates will be plotted against reference T_1 values. As a reference, the T_1 values obtained by the manufacturer with a 1.4T minispec relaxometer are taken (red data in figure 3.7). A linear relation will be fitted to the data.

4

Results

In this chapter, results of two experiments related to 3D acquisition and an experiment to validate signal intensity conversion for quantification of MBF are presented. All shown scans were performed on a 3T scanner (Philips Ingenia, Best, the Netherlands).

In order to perform a low-resolution followed by a high-resolution 3D acquisition during diastole, the scan parameters given in tables 3.2 and 3.1 were selected to minimize the acquisition duration. As explained in section 3.3.1, additional oversampling in slice direction was required to prevent appearance of fold-over artifacts. By determining the excitation pulse shape and oversampling factor that allow acquisition of as few k_z samples as possible without resulting in fold-over, the acquisition duration can be further minimized. To establish the minimum suitable slice oversampling factor, the intensity in a homogeneous phantom was analyzed as a function of slice index. Because only the contrast and no high resolution were required for this purpose, solely the interleaved training profiles of the second imaging stack (shown in Figure3.3) were used for reconstruction. In the next section, the results are given.

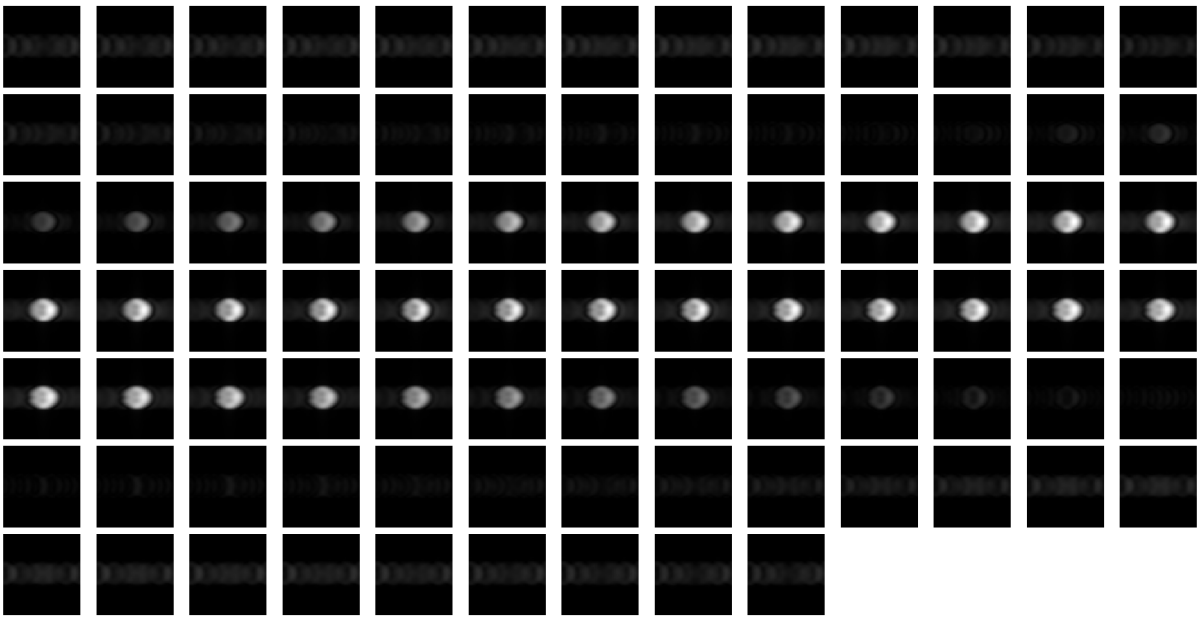

Figure 4.1: Reconstructions of 29 oversampled slices, 29 slices of the field of view, and 29 oversampled slices. Obtained by applying an inverse Fourier transform to the interleaved training data of one dynamic of the second imaging stack.

4.1. Determination of slice oversampling

Figure 4.1 shows the reconstructions of all 87 slices of the experiment. The horizontal axis corresponds to the y or phase encoding direction, of which only a maximum of 11 samples have been acquired in the center of k-space. The vertical axis is along the read-out direction, counting 168 acquired samples. Figure 4.2 shows the average intensity of the ROI as a function of slice index for the spredrex pulse. This is the default excitation pulse, of which the amplitude modulation shape is displayed in Figure 4.3 (the pulse only modulates the amplitude of the carrier wave and not the frequency). Plots for different excitation pulses are included in appendix A, as well as the AM shapes of the pulses. To make the figures comparable, the same scaling of the y axes was used.

Dashed lines indicate the borders of the FOV and red lines are placed 5 slices in front of this border (slice -19) and 4 slices after it (slice 19). The intensity values measured in these slices are 42.2 and 39.6 respectively (in arbitrary units) and these are the first intensities below the local maxima at slices 35 and -35. For all investigated excitation pulses, index 19 and -19 were the first slices for which the average intensity has dropped below the value of the local maximum (see figures A.1 to A.6). The region between slices -19 and 19 was therefore selected as the region to be sampled. It counts 38 slices and corresponds to an oversampling factor of 1.31. As the choice of excitation pulse among the available pulses proved not to influence the minimum slice oversampling, the default spredrex pulse remained the excitation pulse.

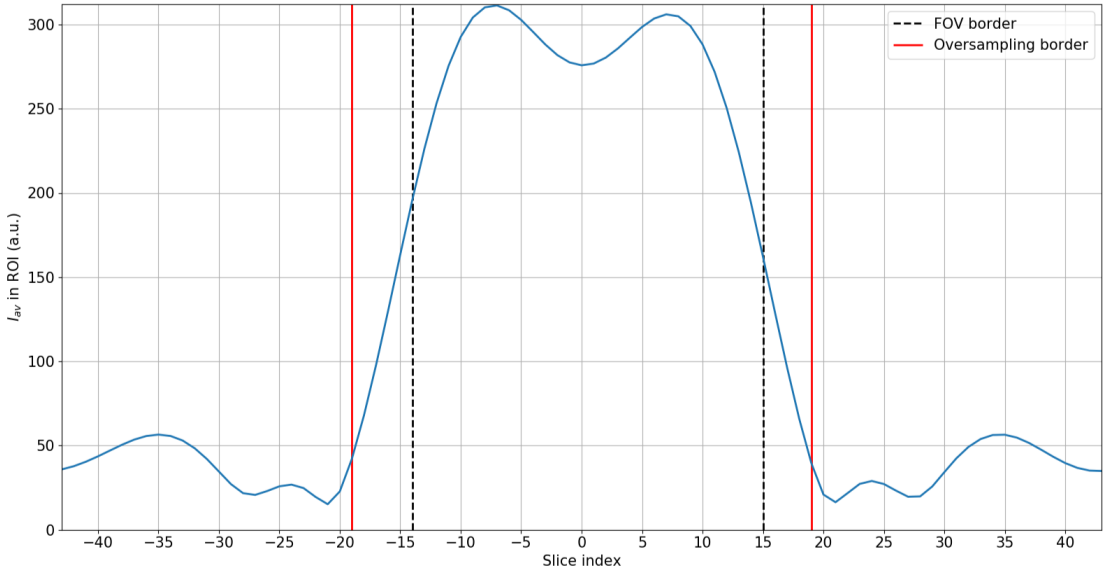

Figure 4.2: Average intensity in the ROI as a function of slice index for the spredrex excitation pulse. The borders of the FOV of 29 slices are marked by the dashed lines and the selected region to be sampled is indicated by red lines. This region includes 5 extra slices on the left side and 4 on the right side.

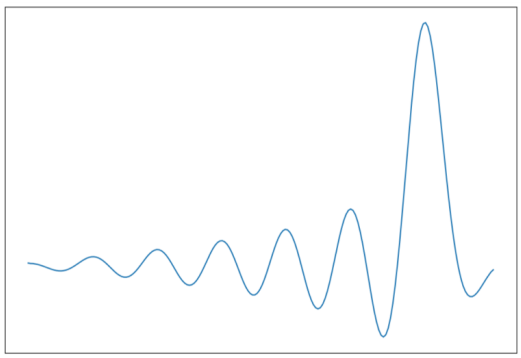

Figure 4.3: Amplitude modulation shape of the spredrex pulse.

4.2. In vivo results

The developed 3D myocardial perfusion sequence with 1.31x slice oversampling and the spredrex excitation pulse was tested in a healthy volunteer (male, 29 years old), without the use of contrast enhancement or saturation preparation. Specifically, without contrast enhancement, magnetization saturation would result in low signal intensities and low contrast, impeding the assessment of the resolution and ability to extract the signal of the LV blood pool and myocardium. Moreover, a sufficient signal-to-noise ratio is required for validation of the reconstruction algorithm.

The resulting scanner reconstructions of the low resolution AIF stack and registered high-resolution second stack are shown in figures 4.4 and 4.5. The phase (y) and frequency (x) encoding directions are indicated. The direction with the smallest body dimension in short-axis view is selected for phase encoding. This approach minimizes phase aliasing artifacts.
In the low-resolution images of Figure 4.4, especially when compared to the high-resolution images for reference, the heart can be distinguished from other anatomical structures and the left and right ventricle can just be discerned. However, the myocardium and LV blood pool are not distinguishable in these images. The use of a contrast agent, causing the right ventricle, left ventricle, and myocardium to brighten consecutively, is expected to solve this issue. Moreover, the raw data reconstructions obtained with a self-supervised learning algorithm by collaborators are anticipated to be of higher quality than the in-line scanner reconstructions. At the time of writing, these reconstructions were still in progress and could not yet be included in this report.
The apical slices of the second stack show no artifacts, for example blurring as a result of respiratory motion. From slice 19 onwards towards the base, however, an artifact appears, as indicated by a white arrow in Figure 4.5. This artifact is attributed to the high undersampling rate.

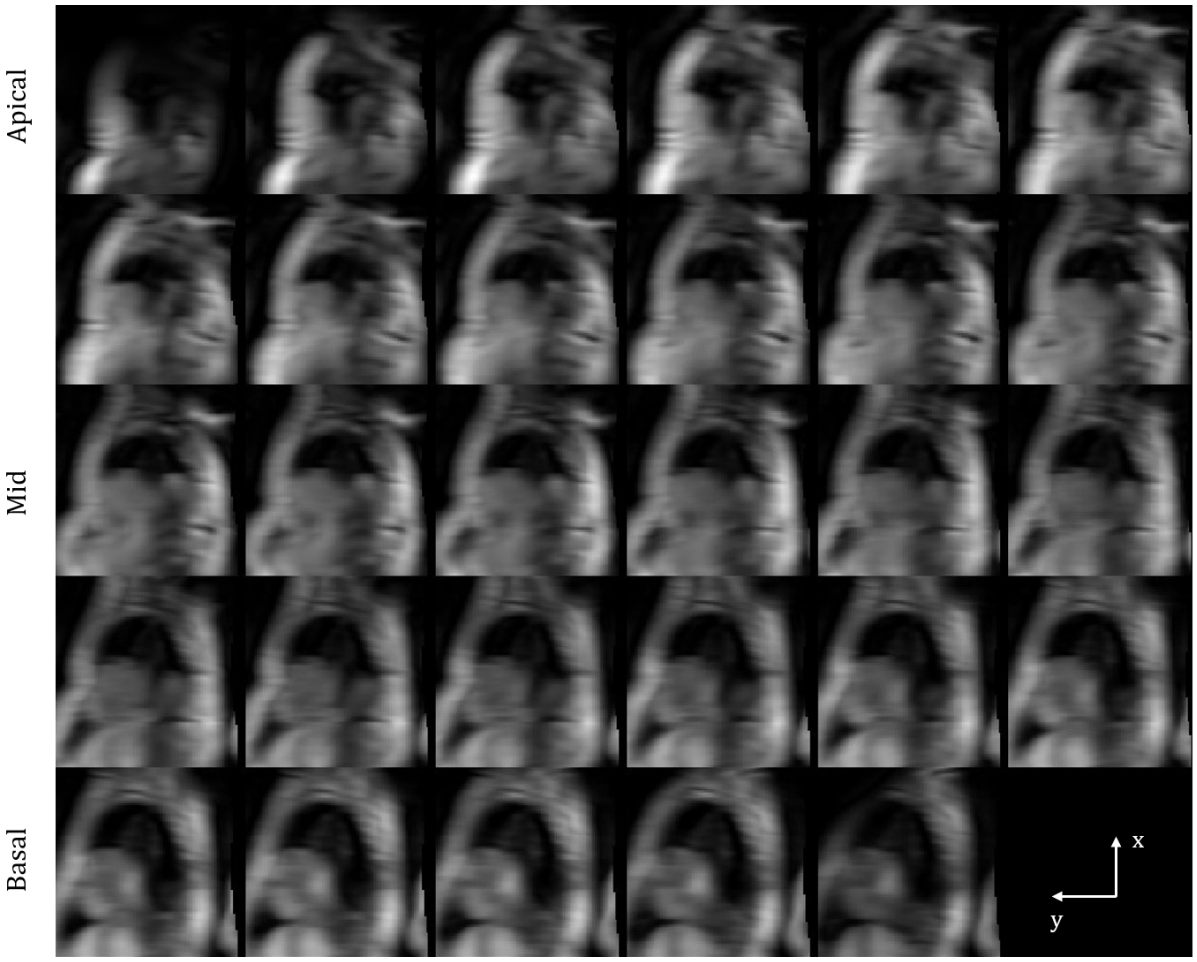

Figure 4.4: Cardiac short axis scans from the first scanning stack, showing the acquired 29 slices. The images were acquired using the procedure and parameters described in section 3.1, except without a saturation prepulse. The images were reconstructed in-line by the scanner and show the heart from apex to base from top-left to bottom-right.

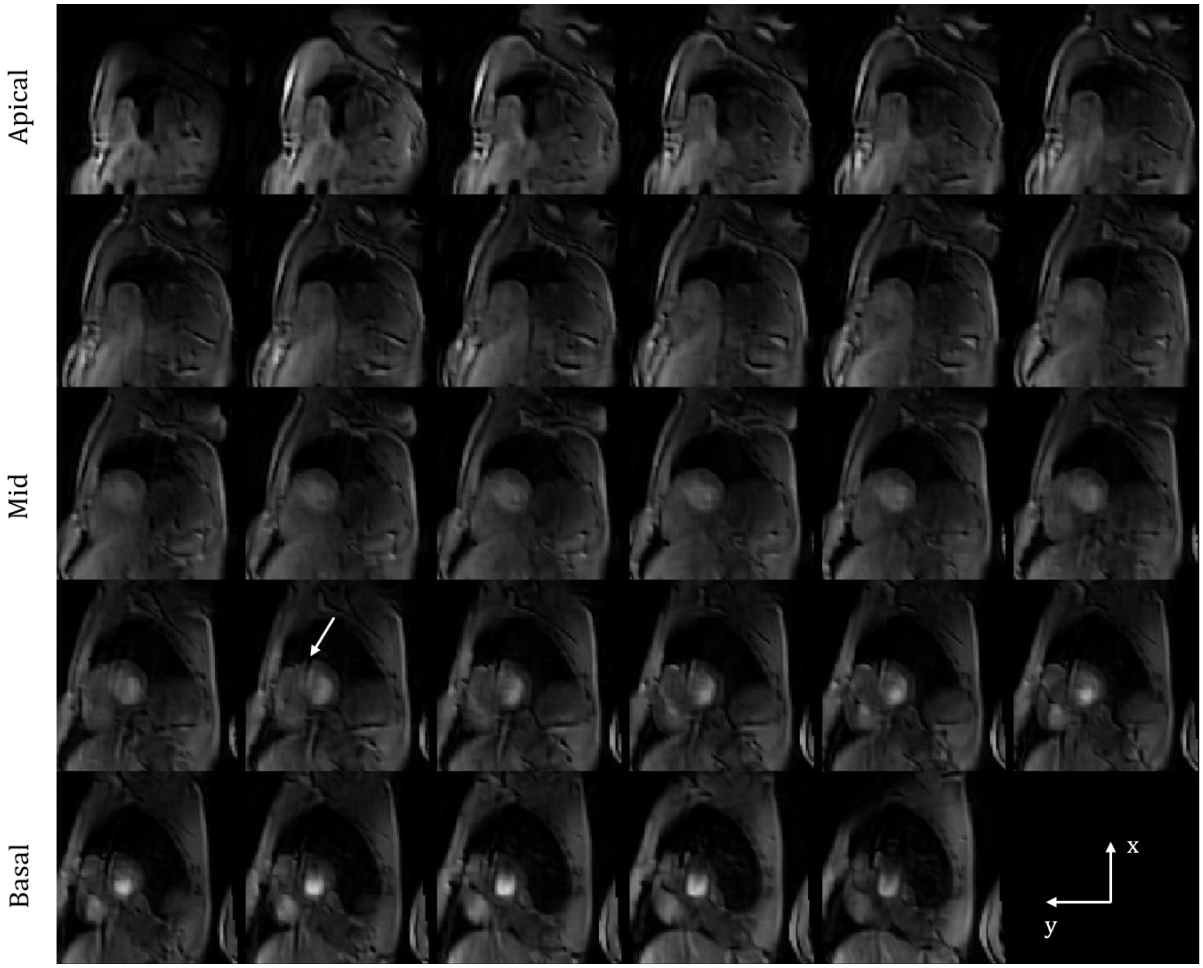

Figure 4.5: Cardiac short-axis scans from the myocardial imaging stack, showing the acquired 29 slices. The images were reconstructed in-line by the scanner and registered pairwise to the first dynamic. The images from top-left to bottom-right show the heart from apex to base.

Figure 4.6 demonstrates the effect of image registration. It shows the target image of the first dynamic and images of the 4 subsequent dynamics, before and after pairwise registration. Also the normalized intensity differences between target and source images and between target and registered images are shown.

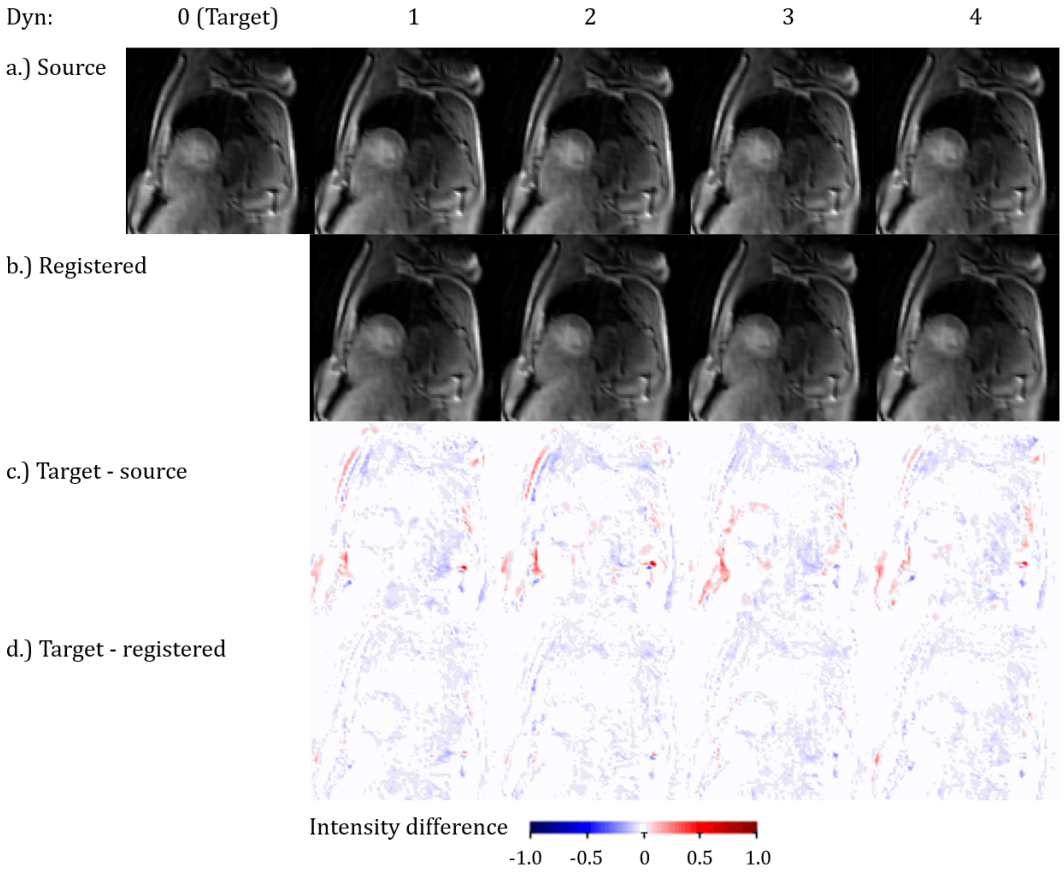

Figure 4.6: Cardiac short-axis scans of the 14th slice from the myocardial imaging stack before (a.) and after (b.) image registration. The images were acquired in 5 subsequent R-R intervals, reconstructed in-line by the scanner and registered pairwise to the target image of the first dynamic by Yi Zhang. The normalized intensity differences between the target and source images (c.) and between the target and registered images (d.) are included as well.

4.3. Quantification: single-point T1 estimation

In this section, we present the results of the experiment to validate the single-point T_1 measurement approach, described in sections 2.6.1 and 3.4. Figure 4.7 and 4.8 show PD-weighted and T_1-weighted images of the T1MES phantom scanned with the developed 3D perfusion sequence. The T_1-weighted and PD-weighted scans were acquired separately. Intensity scaling for visualization purposes of the scans has been taken into account. The left images correspond to the undersampled first stack and the right images to the second stack. The reduction of k-space profiles in phase direction and increased sampling rate for read-out result in a strongly anisotropic resolution of the AIF images.

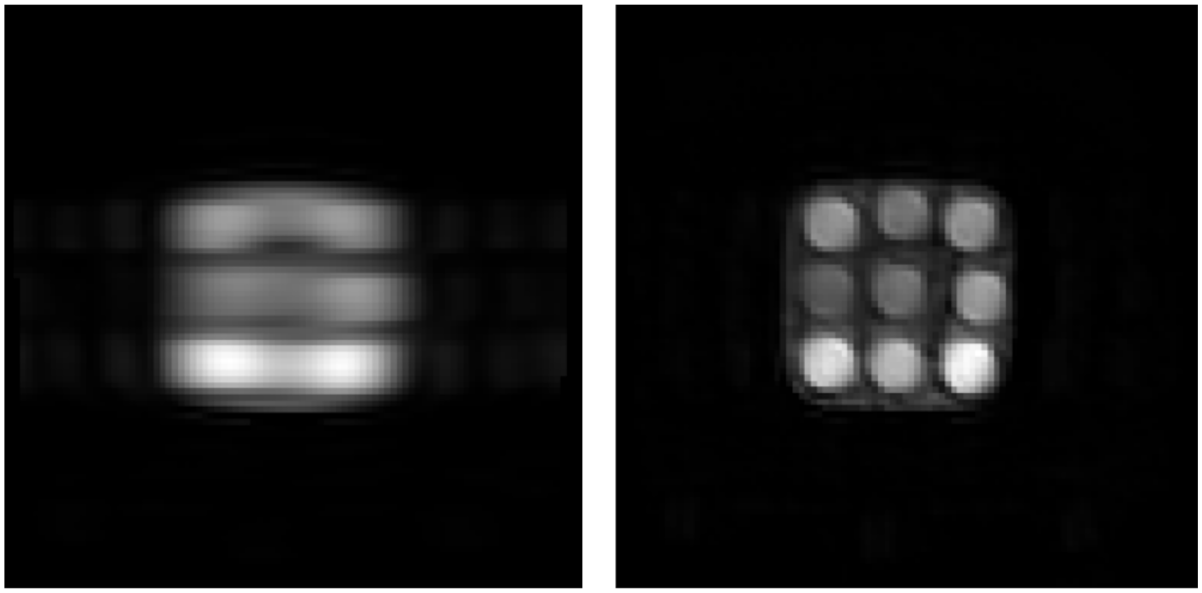

Figure 4.7: PD-weighted scans of the T1MES phantom, reconstructed by the scanner. The images correspond to the fifth slice of the first and second imaging stack respectively. The scan parameters settings can be found in tables 3.2 and 3.1.

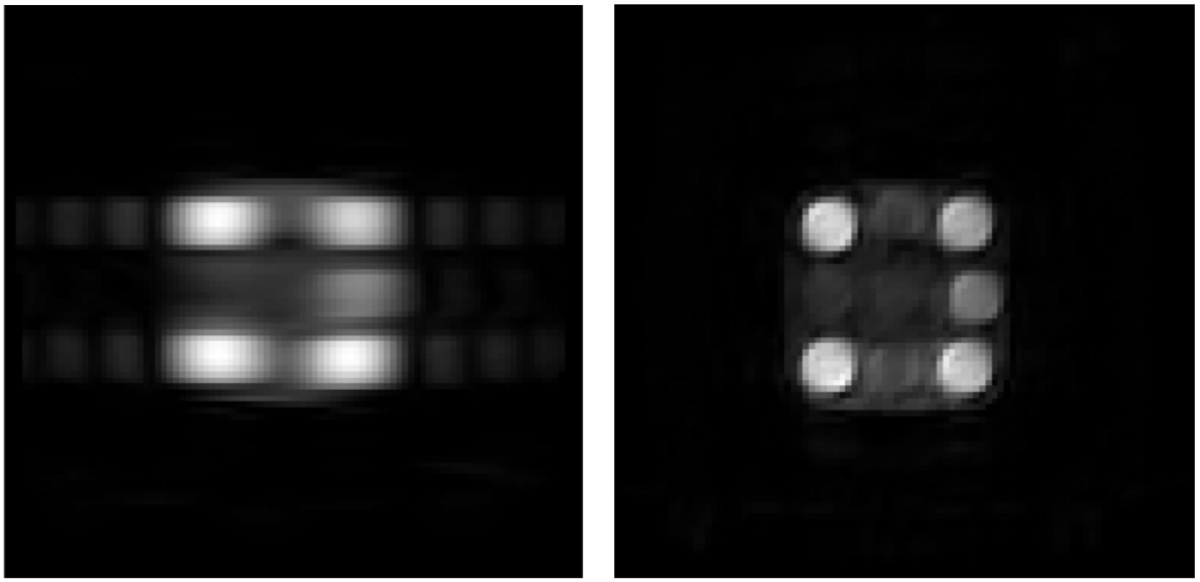

Figure 4.8: T1-weighted scans of the T1MES phantom, reconstructed by the scanner. The images correspond to the fifth slice of the first and second imaging stack respectively. The scan parameters settings can be found in tables 3.2 and 3.1.

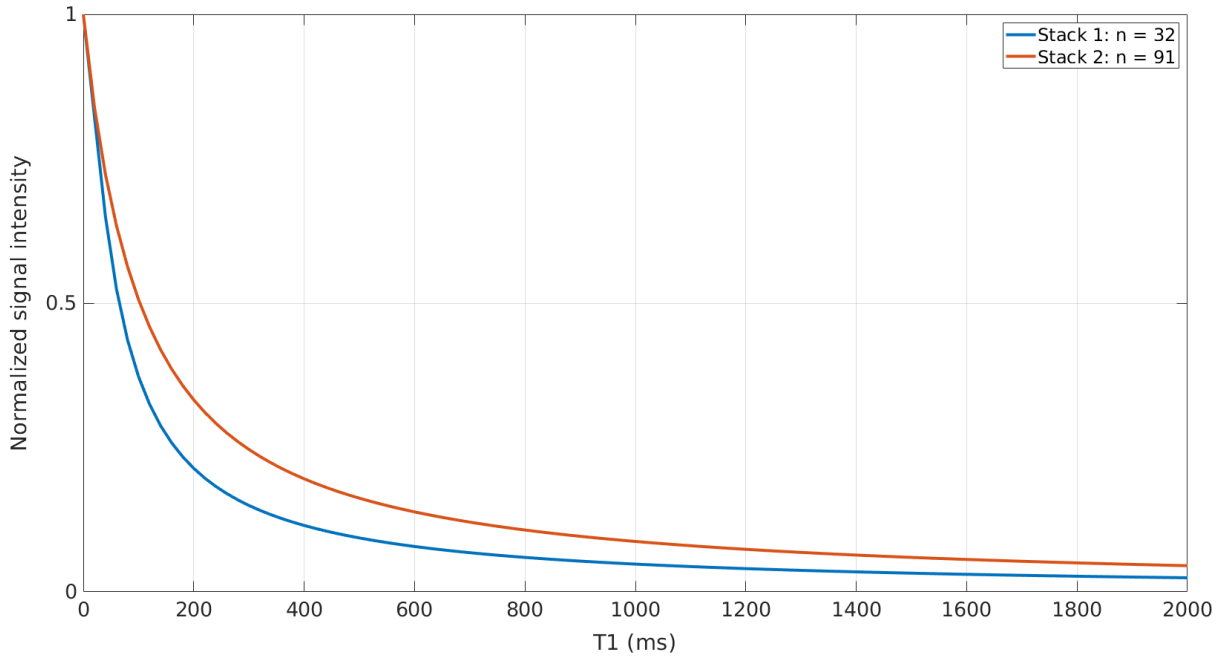

Figure 4.9: Plot of the relation between the normalized signal intensity and T_1 for the scan parameters of stack 1 and 2 listed in tables 3.2 and 3.1.

For the used scan parameters, the theoretical relation between T_1 and the normalized signal intensity, given in equation 2.9, is plotted. A different number of excitation pulses n before acquisition of the center of k-space accounts for the difference between the curves of stack 1 and 2. The normalized intensity expected in images of stack 1 drops more quickly than the intensity of the second stack, because there is less time for T_1 recovery during acquisition of the AIF stack.

Figure 4.10 shows the average T_1 of the $4x4$ ROI that was selected in each vial of images 4.7 and 4.8. The obtained T_1 estimates are plotted against the reference values obtained by the manufacturer of the phantom with a 1.4T relaxometer (red data in Figure 3.7). These reference values are shown in grey, along with the line $y = x$. The standard deviation among the 16 T_1 estimates of each vial is shaded. For vials with higher T_1, the standard deviation is larger, as less magnetization recovery has taken place and the resulting signal is lower. This can be seen in Figure4.8 by comparing the center vial to any of the corner vials. A linear relationship has been fitted to the 5 lowest T_1 estimates, for which no underestimation due to limited recovery time is observed. The obtained slope and intercept for the AIF imaging stack are given by $a_1 = 0.91 \pm 0.004$ and $b_1 = 24 \pm 2$. Estimates of low T_1 values, within the interval $[250, 500]$, can therefore be estimated with relatively good precision and accuracy using the described single-point method. The low-T_1 data of the second imaging stack is best described by a linear function with slope $a_2 = 0.72 \pm 0.004$ and intercept $b_1 = 35 \pm 2$. The recovery rate would, therefore, be consistently underestimated from the myocardial imaging stack.

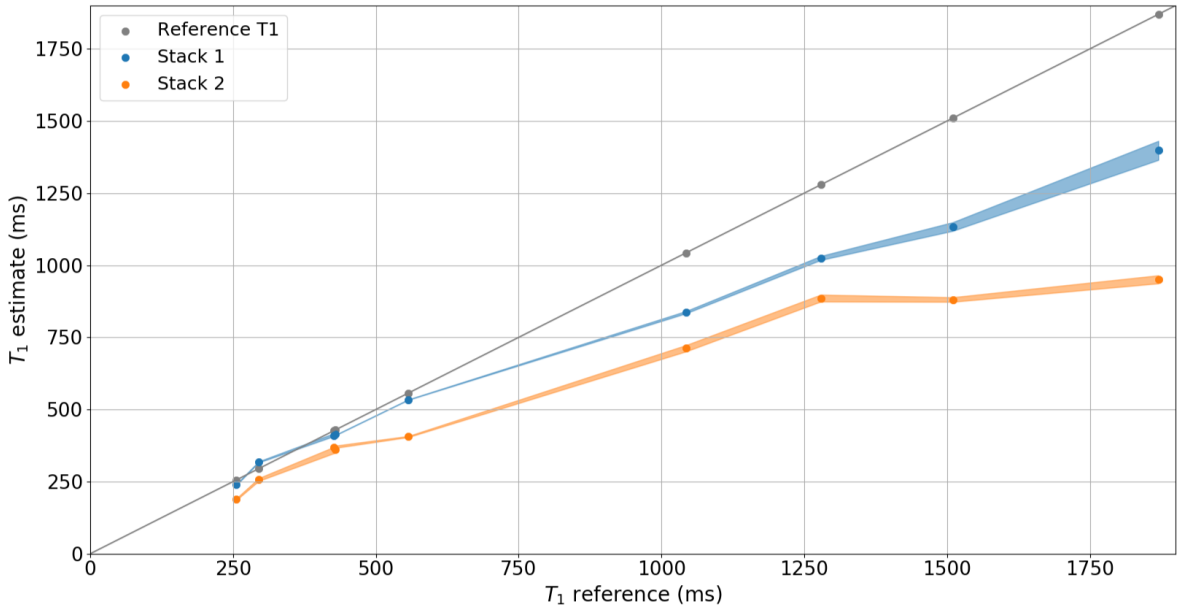

Figure 4.10: Average single-point T_1 estimates of the T1MES phantom plotted against reference T_1 values obtained by the manufacturer using a relaxometer. The standard deviation of the T_1 estimates in the $4x4$ is shaded, in blue for the measurements of stack 1 for the AIF and in orange for stack 2 of myocardial measurement.

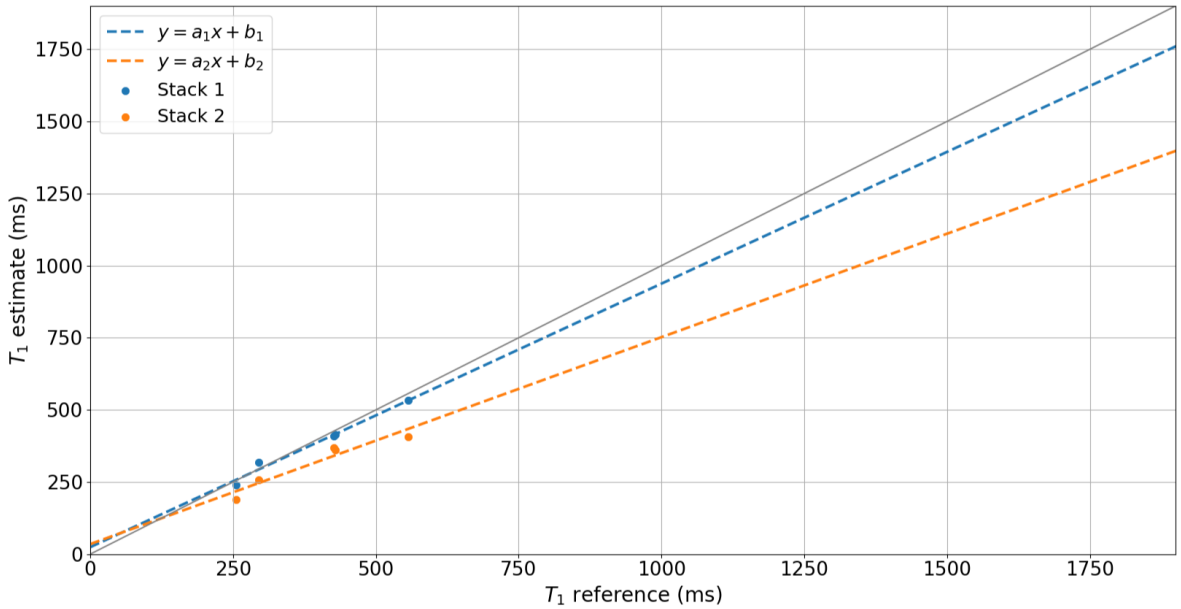

Figure 4.11: Linear least squares approximations to the 5 single-point T_1 measurements with lowest T_1 value from Figure4.10. The approximations are of the form $y = ax + b$ and the obtained fit parameters for the first and second imaging stack (shown in blue and orange respectively) are given by: $a_1 = 0.91 \pm 0.004$, $b_1 = 24 \pm 2$, $a_2 = 0.72 \pm 0.004$, $b_1 = 35 \pm 2$. Reference T_1 values obtained by the manufacturer using a relaxometer were used.

5

Discussion

In this study, we developed a 3D cardiac MR sequence for quantification of myocardial blood flow. Robustness of this sequence to elevated heart rates is important for clinical applicability. Although the targeted isotropic voxel size was 3 mm, this has been increased to 3.6 mm to ensure tolerance to higher heart rates. Currently, the developed 3D myocardial perfusion sequence can be applied when the subject's heart rate does not exceed 76 bpm. At higher heart rates, the R-R interval is not sufficiently long to acquire both the arterial input function and myocardial images. Drawing from experience of a cardiologist with regadenoson-induced stress FPP examinations, tolerance to heart rates up to 80 bpm is feasible. Ideally, the acquisitions would be further accelerated. Depending on the quality and resolution of reconstructions obtained by the self-supervised learning algorithm, fewer encoding steps in slice or phase direction can potentially be used. This could entail either reducing the number of low frequency samples of the training stage, or the highest frequency of the undersampling stage, but would compromise the image quality.
A reduction in slice encoding steps from 7 to 5 or 3 for the AIF is expected to be possible without a significant impact on the extraction of the AIF, as essentially only one slice in the left ventricle is required. However, it would reduce the signal strength and ability to estimate high T_1, as the longitudinal magnetization will have less time to recover, and it may impede the extraction of the coil sensitivities.

The experiment for single-point T_1 measurement in phantom shows potential for obtaining accurate T_1 estimates up to approximately 500 ms from 3D first-pass myocardial perfusion scans. High T_1 values are underestimated, due to limited delay and saturation times (TD = 5.74 ms, TS = 64.9 for the AIF stack, TS = 177.0 for the main imaging stack). In [7], where 2D slices were imaged with a delay time of TD = 75 ms, no underestimation of high T_1 values was observed. Removal of the second saturation pulse before the myocardial imaging stack increases the delay time to TD = 161 ms and results in a saturation time of TS = 312 ms. The magnetization of contrast-enhanced blood with T_1 = 250 ms would then have recovered to 71% of its initial value. To achieve accurate estimation of T_1 from the second imaging stack across the entire spectrum of values encountered in a contrast-enhanced examination, ranging from approximately 250 to 1900 ms, we, therefore, suggest the use of a single saturation pulse. Solving the underestimation of high T_1 values from the AIF images as well is more difficult, as a delay after saturation would have to be included, increasing the sequence duration.

The estimates of low T_1 from the AIF stack are in good agreement with reference values, while the estimates of the myocardial imaging stack are consistently below reference and would require correction by a factor 1.40, as obtained from the slope of the linear fit. The underestimation of T_1 from the second imaging stack is attributed to the fact that solely the recovery of the longitudinal magnetization is modelled. Factors such as the slice excitation profile and T_2^* dephasing are neglected. Also transfer of magnetization is not accounted for. This is a process in which energy deposited by off-resonance RF excitation to bound protons is transferred to protons in free fluid via dipole-dipole interactions [10]. The magnetization of free protons becomes partially saturated and the signal will be lower than anticipated. In the second imaging stack, which involves a longer train of excitation pulses compared to the first, these contributions accumulate to a deviation in magnetization evolution from the model.
The fact that the PD-weighted and T_1-weighted images of this experiment were acquired as separate, con-

secutive scans is not expected to influence the T_1 estimates. If it had an influence, the values of both stacks would be affected, yet the low T_1 estimates of the AIF stack form a good approximation of the reference values.
For more accurate estimation of T_1 from the high-resolution imaging stack, Bloch simulations of the imaging sequence can be performed, modelling both the longitudinal magnetization evolution and transverse magnetization between spoiling events and incorporating the slice excitation profile [26].

The quantification procedure can be further modified for the case when a contrast agent is administered and T_2^* related signal loss in the LV blood pool is expected to be of concern. Although clipping of the AIF is prevented by a short acquisition duration, decrease of T_2^* will still have a significant influence on the measured intensity. By means of a phantom experiment with different contrast agent concentrations, Kellman et al. showed that correction of T_2^* led to an approximately 10% higher [Gd] for the AIF [26], using very similar parameters for AIF measurement (TE = 0.76 ms, TR = 2.45 ms and α_{T1} = 5°, compared to TE = 0.73 ms, TR = 1.90 ms and α_{T1} = 4° in this work). This indicates that underestimation of [Gd] is to be expected for the perfusion sequence developed in this project. T_2^* can be estimated by using dual-echo acquisition for the AIF and fitting the measurements to the exponential decay curve of equation 2.4 [26, 46].

Further steps in the process towards obtaining myocardial blood flow maps include patient scanning with contrast enhancement and application of a blood-tissue exchange model after the left ventricle and myocardium are segmented and the signals have been converted to tracer concentrations. Ultimately, the goal in quantitative myocardial perfusion imaging would be to perform all the steps as shown in figure 1.1 inline on the scanner such that the procedure can be easily included in the clinical workflow. This requires more research and development, but is not deemed impossible.
Quantification of myocardial blood flow from 3D balanced steady-state free precession (b-SSFP) acquisitions may be an interesting parallel line of research to pursue. These type of gradient echo sequences provide higher SNR than spoiled GRE and are therefore mainly used for visual assessment of myocardial perfusion in the clinic. An already existing procedure that is familiar to clinicians could that way be extended with quantitative assessment. A disadvantage of b-SSFP sequences that should be named is sensitivity to B_0 and B_1 inhomogeneity, possibly resulting in artifacts [24], especially at low flip angles [26]. When using a 1.5T scanner, the artifacts are significantly reduced. The field inhomogeneity of a 1.5T and a 3T scanner is comparable in parts per million (in the order of 1), but is lower in an absolute sense for a low-field scanner [18].
Where in this project a cartesian sampling pattern with acceleration is used for 3D CMR, radial or spiral readout is also promising for this application as naturally higher sampling rates are provided for low frequencies. In a recent study by Mendes et al., a 3D radial stack-of-stars readout in combination with 2D AIF acquisition basal to the 3D readout was successfully used for perfusion quantification. In this study, relation 2.9, adapted for radial readout, was also applied to estimate T_1. A downside of radial sampling compared to cartesian sampling is the complexity it adds to the reconstruction problem.
For increasing diagnostic confidence of perfusion imaging with cardiac MR, Simultaneous Multislice imaging (SMS) forms a midway between conventional low-coverage 2D perfusion imaging and highly accelerated 3D perfusion imaging. This technique is considered worth further exploring and implementing, as it allows imaging of multiple slices within the same time compared to standard single-slice acquisition, resulting in increased coverage without increased acquisition duration. SMS has been applied to spoiled gradient echo sequences [48, 52] and was recently combined with balanced SSFP sequences for first-pass perfusion imaging as well [30]. Quantification of myocardial blood flow using simultaneous multislice imaging is not yet widely studied.

6

Conclusion

A dual sequence for free-breathing, first-pass myocardial perfusion imaging in 3D has been developed for quantification of myocardial blood flow. Scan parameters were optimized to reduce the acquisition duration and thereby mitigate the effects of cardiac motion, prevent the appearance of fold-over artifacts, and maintain sufficient resolution. Acquisition of proton density-weighted images for normalization of the arterial input function and myocardial signal was incorporated in the scanning sequence. Collaborations were established for image reconstruction and image registration using deep learning.

A validation study in vivo, without contrast enhancement, was conducted to confirm the adequacy of AIF acquisition for distinguishing the left ventricular blood pool and to assess the robustness of the sequence to motion and elevated heart rates. Preliminary image reconstructions by the scanner were promising, but an artifact was observed towards the base of the heart due to strongly reduced phase encoding. In reconstructions obtained by means of a deep learning algorithm, such artifacts are expected to be alleviated. The procedure for obtaining a quantitative myocardial blood flow map was investigated, and a method for single-point measurement of T_1 was implemented and tested in a phantom for the developed sequence. Accurate T_1 estimates were achieved in the low-T_1 range (250-500 ms), while longer relaxation times were significantly underestimated. Removal of the second saturation pulse before acquisition of the myocardial signal will increase the highest T_1 value that can be accurately estimated from the myocardial images and is suggested as an improvement to the sequence.

Acknowledgements

During my project, I was guided and supported by many people. First of all, I would like to thank Sebastian Weingärtner and Ayda Arami for giving me the opportunity to work on 3D Perfusion in Mars Lab and for supervising me. Thank you, Ayda, for taking the time to meet with me twice a week and giving me advice, especially from a clinical perspective, which was new to me. Thank you both for the encouragement, the useful discussions and valuable feedback. The support from the entire Mars Lab was also much appreciated. Furthermore, I would like to thank Yi Zhang, dr. Qian Tao, Christal van de Steeg-Henzen, Mert Acar and dr. Mehmet Akçakaya for their collaboration on this project.
Dr. Alexandru Cernicanu and dr. Peter Kellman shared some of their expertise on quantitative perfusion imaging with us, which I would also like to acknowledge.
I would like to thank Gijs, Hanna and the other students of room D207 and in particular my friends Maaike and Esther for making the time in the far end of the physics building more enjoyable. Finally, I would like to thank my family and especially my boyfriend Wouter and sister Jolien for their unconditional support.

A

Slice excitation profiles

In this appendix the measured slice profiles of several of excitation pulses are given, combined with the amplitude modulation shapes of the pulses.

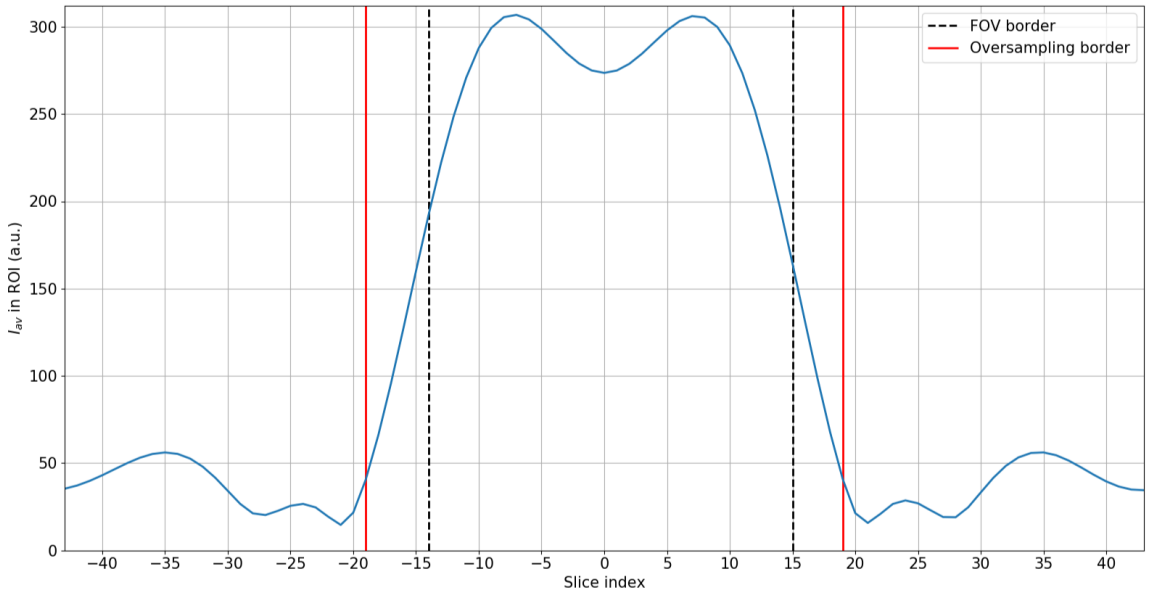

Figure A.1: Average intensity in the ROI as a function of slice index for the optimum excitation 1 pulse. The borders of the FOV of 29 slices are marked by dashed lines and the selected region to be sampled is indicated by red lines. This region includes 5 extra slices on the left side and 4 on the right side.

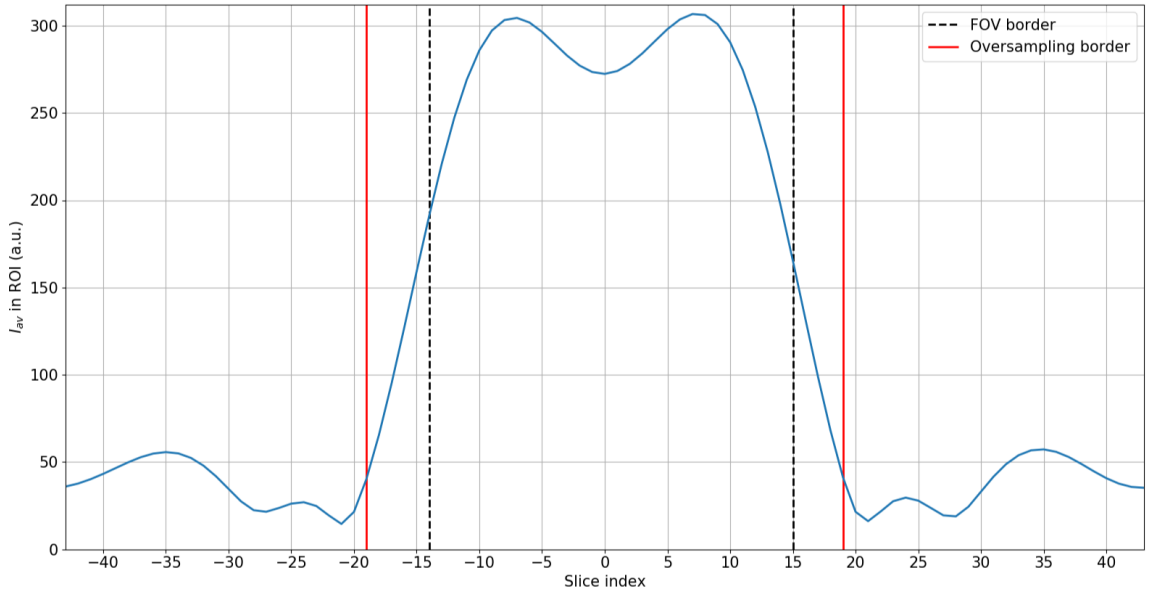

Figure A.2: Average intensity in the ROI as a function of slice index for the optimum excitation 2 pulse. The borders of the FOV of 29 slices are marked by dashed lines and the selected region to be sampled is indicated by red lines. This region includes 5 extra slices on the left side and 4 on the right side.

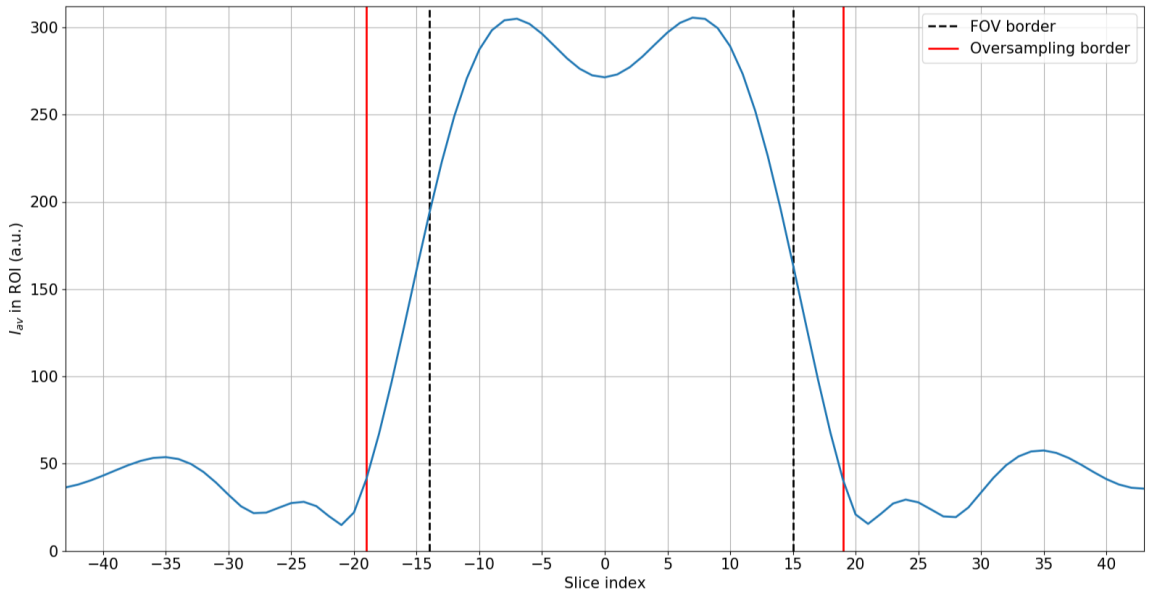

Figure A.3: Average intensity in the ROI as a function of slice index for the xerderps excitation pulse, the time reversed spredrex pulse. The borders of the FOV of 29 slices are marked by dashed lines and the selected region to be sampled is indicated by red lines. This region includes 5 extra slices on the left side and 4 on the right side.

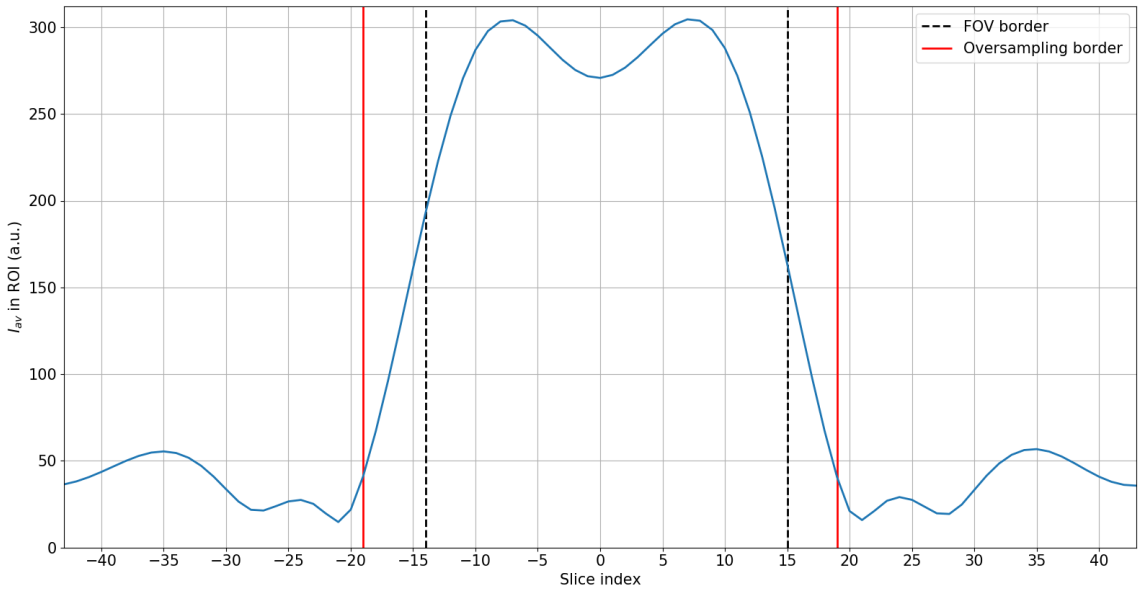

Figure A.4: Average intensity in the ROI as a function of slice index for a block excitation pulse. The borders of the FOV of 29 slices are marked by dashed lines and the selected region to be sampled is indicated by red lines. This region includes 5 extra slices on the left side and 4 on the right side.

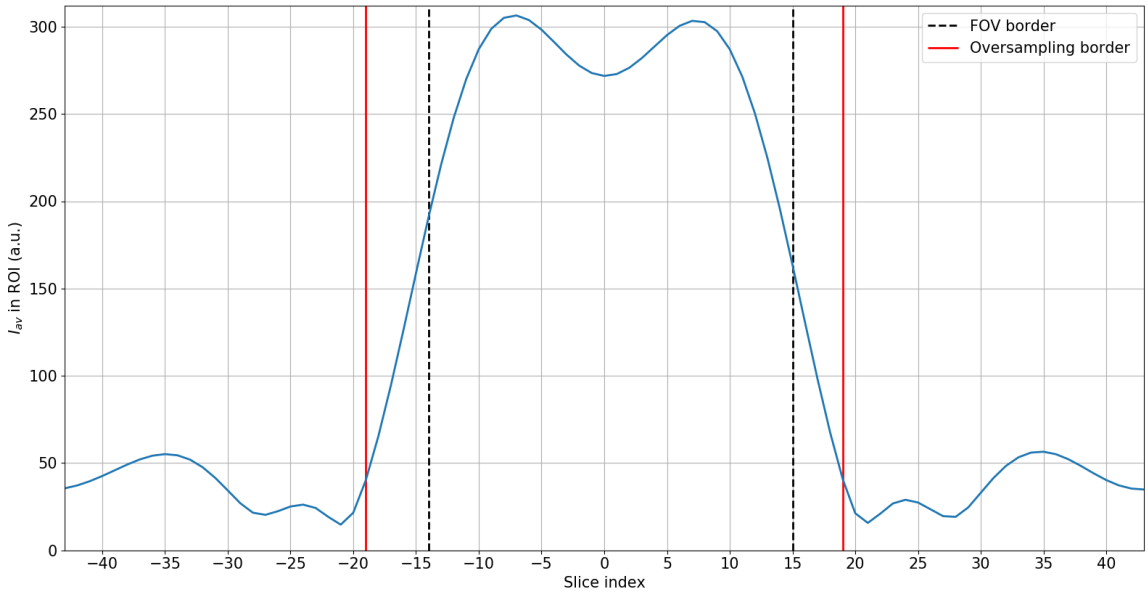

Figure A.5: Average intensity in the ROI as a function of slice index for the spectex excitation pulse. The borders of the FOV of 29 slices are marked by dashed lines and the selected region to be sampled is indicated by red lines. This region includes 5 extra slices on the left side and 4 on the right side.

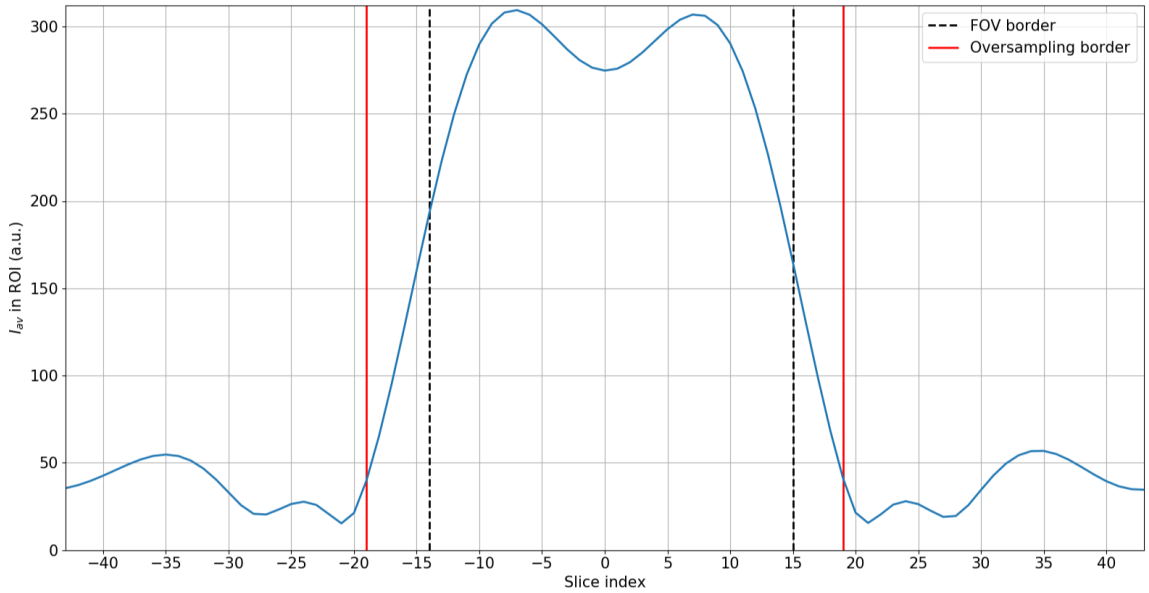

Figure A.6: Average intensity in the ROI as a function of slice index for the sg 100 100 excitation pulse. The borders of the FOV of 29 slices are marked by dashed lines and the selected region to be sampled is indicated by red lines. This region includes 5 extra slices on the left side and 4 on the right side.

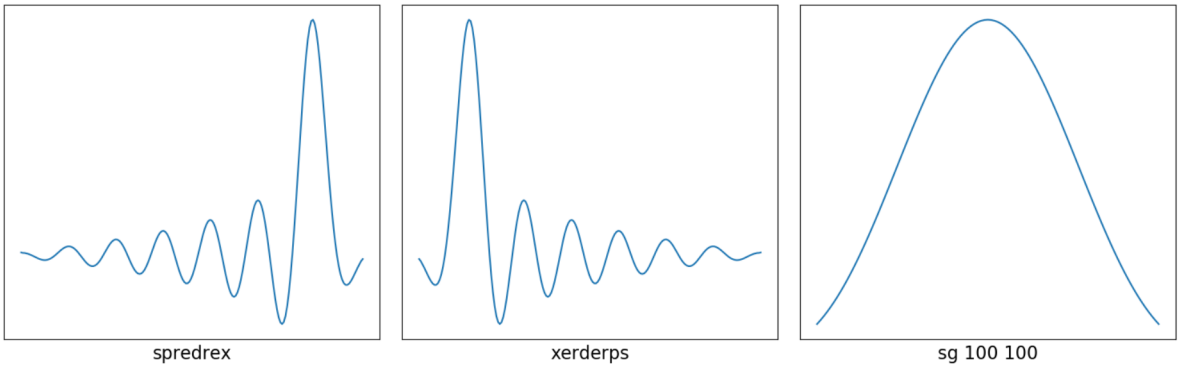

Figure A.7: Amplitude modulation shape of the spredrex, xerderps and sg 100 100 excitation pulses.

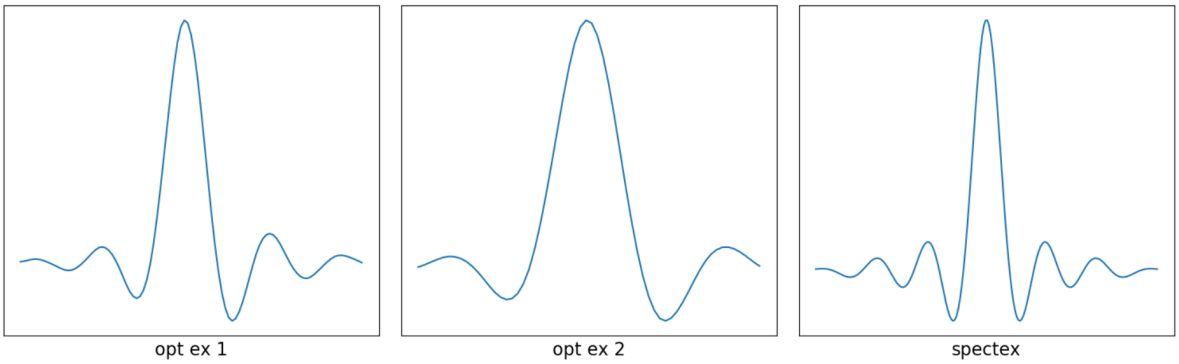

Figure A.8: Amplitude modulation shape of the optimum excitation 1, optimum excitation 2 and spectex excitation pulses.

B

Working with Philips raw scan data

When exporting raw scan data from a Philips MR scanner, three files containing all the information of the scan are created. The extensions of the files are .raw, with the raw data, .lab, with the data labels and .sin, with the values of the scanning parameters. The raw data we read and sort from these files using MRecon, an object-oriented Matlab library by Gyrotools [19].

After opening the Philips raw data files with MRecon and reading the data, a number of corrections need to be applied before k-space data is obtained that can be reconstructed with an inverse Fourier transform. The data may contain magnitude and phase offsets for example. The corrections that are applied before sorting the data and exporting it as a k-space matrix are a nonlinearity correction, a random phase and a measurement phase correction, a DC offset correction and a PDA correction. If desired, the oversampling can also be removed first. Especially the random phase correction is very important, as it subtracts a random phase that was added to every acquired profile by the receiver to reduce artifacts. Without this correction, the data is randomly distributed in phase direction. More information on the raw data corrections can be found in [28].

C

Simultaneous multislice imaging

Diagnostic accuracy of first-pass myocardial perfusion imaging with MRI as currently applied in the clinic is limited by low myocardial coverage. The main technique for increasing myocardial coverage that was investigated and developed in this project is 3D cardiac MRI. Besides 3D imaging, 2D Simultaneous Multislice imaging (SMS) enables acquisition of more cardiac slices in each R-R interval. By exciting and acquiring N separated slices simultaneously with a multiband RF pulse, the acquisition time can be reduced by a factor N. In this master thesis, an initial attempt to implement SMS has been made, as it is currently only available for brain imaging with $N = 2$ in most scanners.

A multiband RF pulse for exciting N slices, each with complex phase ϕ_n and frequency offset $\Delta\omega_n$, can be written as:

$$RF_{MB}(t) = A(t) \cdot \sum_{n=1}^{N} e^{i\Delta\omega_n t + \phi_n}, \tag{C.1}$$

in which $A(t)$ is the complex RF waveform of a single slice [31].

In order to resolve the images of the different simultaneously excited slices, the slice images will be shifted with respect to each other along the phase encoding direction. An intuitive method which allows direct reconstruction of the slice images would be to increase the phase FOV by roughly a factor N. This is referred to as the Phase-Offset MultiPlanar (POMP) method and was proposed in 1991 [17]. When using POMP, however, the scan time is not reduced, as more phase encoding lines are required for the extended FOV. With the introduction of parallel imaging, this problem could be solved by using coil sensitivity information for unaliasing the images. This is done in CAIPIRINHA, Controlled Aliasing in Parallel Imaging Results in Higher Acceleration, introduced by Breuer et al. [4].

C.1. Phase cycling for controlled aliasing

To determine the required operation to achieve a shift along the phase encoding direction, the following property of the Fourier transform is of importance:

$$x(y - y_0) \xrightarrow{\mathcal{F}} s(k_y) e^{-2\pi i k_y y_0} \tag{C.2}$$

For cardiac application, we focus on the case $N = 3$. If a multiband pulse excites 3 slices simultaneously and one band should be shifted by $+FOV_y/3$ and another by $-FOV_y/3$ along the y-axis, the following relations can be used to determine how the RF pulse needs to be adapted:

$$k_y = n\Delta k = \frac{n}{N\Delta y} = \frac{n}{FOV_y} \tag{C.3}$$

To shift two of the three bands outwards in image space, the Fourier data of these bands need factors $e^{-2\pi i n/3}$ and $e^{2\pi i n/3}$, where $n \in [1, N]$ indicates the profile number. This additional phase can be transmitted by the

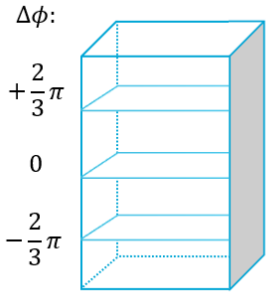

Figure C.1: Overview of phase increments $\Delta\phi$ required to separate the 3 slices by $FOV_y/3$ in the image.

$\mathbf{B_1}$-field. By cycling the phase $\phi_n = n\Delta\phi$ of two of the RF bands cycle with increments $\Delta\phi = \frac{2}{3}\pi$ and $\Delta\phi = -\frac{2}{3}\pi$, the bands will obtain the desired phase shift. In total, there are three different combinations of RF phases, so three different multiband pulses are required.
The framework design and initial coding phase for computation of the multiband pulses and cycling were completed. The validation phase of the implementation was still in progress, so no results of SMS imaging could be included in this report.

Bibliography

[1] G. Balakrishnan, A. Zhao, M.R. Sabuncu, J. Guttag, and A.V. Dalca. Voxelmorph: A learning framework for deformable medical image registration. *IEEE Transactions on Medical Imaging*, 38(8):1788–1800, 2019.

[2] T.M. Bateman, G.V. Heller, A.I. McGhie, J.D. Friedman, J.A. Case, J.R. Bryngelson, G.K. Hertenstein, K.L. Moutray, K. Reid, and S.J. Cullom. Diagnostic accuracy of rest/stress ECG-gated Rb-82 myocardial perfusion PET: Comparison with ECG-gated Tc-99m sestamibi SPECT. *Journal of Nuclear Cardiology*, 13(1): 24–33, 1 2006.

[3] M. Božić-Iven, S. Rapacchi, Q. Tao, I. Pierce, G. Thornton, C. Nitsche, T. A. Treibel, L. R. Schad, and S. Weingärtner. Improved reproducibility for myocardial ASL: Impact of physiological and acquisition parameters. *Magnetic Resonance in Medicine*, 91(1):118–132, 2024.

[4] F.A. Breuer, M. Blaimer, R.M. Heidemann, M.F. Mueller, M.A. Griswold, and P.M Jakob. Controlled aliasing in parallel imaging results in higher acceleration (CAIPIRINHA) for multi-slice imaging. *Magnetic Resonance in Medicine*, 53(3):684–691, 2005.

[5] J.T. Bushberg, J.A. Seibert, E.M.Jr. Leidholdt, and J.M. Boone. *The Essential Physics of Medical Imaging*. Wolters Kluwer Health, Philadelphia, 3rd edition, 2011.

[6] G. Captur, P. Gatehouse, and K.E. Keenan. A medical device-grade T1 and ECV phantom for global T1 mapping quality assurance—the T1 mapping and ECV standardization in cardiovascular magnetic resonance (T1MES) program. *Journal of Cardiovascular Magnetic Resonance*, 18(58), 2016.

[7] A. Cernicanu and L. Axel. Theory-Based Signal Calibration with Single-Point T1 Measurements for First-Pass Quantitative Perfusion MRI Studies. *Academic Radiology*, 13(6):686–693, 6 2006.

[8] A. Chruścik, K. Kauter, L. Windus, E. Whiteside, and C. Freeman. *Physiology I*. Pressbooks, 2021.

[9] A.D. Elster. T2-shortening by Gd. `https://www.mriquestions.com/does-gd-affect-t2.html`, . (Accessed on 20/03/2024).

[10] A.D. Elster. Magnetization transfer. `https://mriquestions.com/magnetization-transfer.html`, . (Accessed on 19/04/2024).

[11] A.D. Elster. Partial fourier techniques. `https://www.mriquestions.com/partial-fourier.html`, . (Accessed on 24/01/2024).

[12] A.D. Elster. Wrap-around artifact. `https://mriquestions.com/wrap-around-artifact.html`, . (Accessed on 12/04/2024).

[13] A.D. Elster. Spoiled gre parameters. `https://www.mriquestions.com/spoiled-gre-parameters.html`, . (Accessed on 18/03/2024).

[14] M.J. Fair, P.D. Gatehouse, E. Reyes, G. Adluru, J. Mendes, T. Khan, R. de Silva, R. Wage, E.V.R. DiBella, and D.N. Firmin. Initial investigation of free-breathing 3D whole-heart stress myocardial perfusion MRI. *Global cardiology science & practice*, 3(38), 2020.

[15] W.F. Fearon. *Chapter 14 - Invasive Testing*. Elsevier, 2018.

[16] T. Fritz-Hansen, J.D. Hove, K.F. Kofoed, H. Kelbaek, and H.B.W. Larsson. Quantification of MRI measured myocardial perfusion reserve in healthy humans: A comparison with positron emission tomography. *Journal of Magnetic Resonance Imaging*, 27(4):818–824, 4 2008.

[17] G.H. Glover. Phase-offset multiplanar (POMP) volume imaging: a new technique. *Journal of Magnetic Resonance Imaging*, 1:457–461, 1991.

[18] M.J. Graves. 3 T: the good, the bad and the ugly. *The British journal of radiology*, 95(1130), 2022.

[19] Gyrotools. Reconframe: Easy-to-use and versatile reconstruction environment for Matlab and Python. `https://www.gyrotools.com/gt/index.php/products/reconframe`.

[20] Y.S. Hamirani and C.M. Kramer. Cardiac MRI assessment of myocardial perfusion. 10(3):349–358, 2010.

[21] L.Y. Hsu, M. Jacobs, M. Benovoy, A.D. Ta, H.M. Conn, S. Winkler, A.M. Greve, M.Y. Chen, S.M. Shanbhag, W.P. Bandettini, and A.E. Arai. Diagnostic Performance of Fully Automated Pixel-Wise Quantitative Myocardial Perfusion Imaging by Cardiovascular Magnetic Resonance. *JACC: Cardiovascular Imaging*, 11 (5):697–707, 5 2018.

[22] F. Ilardi, A. D'andrea, F. D'ascenzi, F. Bandera, G. Benfari, R. Esposito, A. Malagoli, G. E. Mandoli, C. Santoro, V. Russo, M. Crisci, G. Esposito, and M. Cameli. Myocardial work by echocardiography: Principles and applications in clinical practice. *Journal of Clinical Medicine*, 10(19), 10 2021.

[23] IMAIOS. eMRI sequences: Gradient Echo. `https://www.imaios.com/en/e-mri/sequences/gradient-echo`. (Accessed on 18/09/2023).

[24] J. Jang, S. Bellm, S. Roujol, T.A. Basha, M. Nezafat, S. Kato, S. Weingärtner, and R. Nezafat. Comparison of spoiled gradient echo and steady-state free-precession imaging for native myocardial T1 mapping using the slice-interleaved T1 mapping (STONE) sequence. *NMR in Biomedicine*, 29(10):1486–1496, 10 2016.

[25] M. Jerosch-Herold, A.E. Stillman, and N. Wilke. Magnetic resonance quantification of the myocardial perfusion reserve with a fermi function model for constrained deconvolution. *Medical Physics*, 25:73–84, 1998.

[26] P. Kellman, M.S. Hansen, S. Nielles-Vallespin, J. Nickander, R. Themudo, M. Ugander, and H. Xue. Myocardial perfusion cardiovascular magnetic resonance: optimized dual sequence and reconstruction for quantification. *Journal of cardiovascular magnetic resonance*, 19, 2017.

[27] W. Lepper, T. Belcik, K. Wei, J. R. Lindner, J. Sklenar, and S. Kaul. Myocardial contrast echocardiography. *Circulation*, 109(25):3132–3135, 2004.

[28] GyroTools LLC. MRecon documentation: methods. `https://docs.gyrotools.com/mrecon/latest/src/mrecon/methods.html`, 2021. (Accessed on 28/03/2024).

[29] MathWorks. fzero: root of nonlinear function. `https://nl.mathworks.com/help/matlab/ref/fzero.html`. (Accessed on 20/03/2024).

[30] S. McElroy, G. Ferrazzi, M.S. Nazir, K.P. Kunze, R. Neji, P. Speier, D. Stäb, C. Forman, R. Razavi, A. Chiribiri, and S. Roujol. Combined simultaneous multislice bSSFP and compressed sensing for first-pass myocardial perfusion at 1.5 T with high spatial resolution and coverage. *Magnetic Resonance in Medicine*, 84(6): 3103–3116, 12 2020.

[31] S. Moeller and S. Banerjee. *Chapter 7 - Simultaneous Multislice Reconstruction*, volume 7 of *Advances in Magnetic Resonance Technology and Applications*. Academic Press, 2022.

[32] M. Naghavi, H. Wang, C. Allen, R.M. Barber, Z.A. Bhutta, A. Carter, D.C. Casey, F.J. Charlson, A.Z. Chen, and M.M. Coates. Global, regional, and national life expectancy, all-cause mortality, and cause-specific mortality for 249 causes of death, 1980–2015: a systematic analysis for the global burden of disease study 2015. *The lancet*, 388(10053):1459–1544, 2016.

[33] M.A. Perazella. Gadolinium-contrast toxicity in patients with kidney disease: nephrotoxicity and nephrogenic systemic fibrosis. *Current drug safety*, 3(1):67–75, 2008.

[34] J.L. Prince and J.M. Links. *Medical Imaging Signals and Systems*. Pearson, 2nd edition, 2015.

[35] A.A. Qayyum and J. Kastrup. Measuring myocardial perfusion: The role of PET, MRI and CT, 6 2015.

[36] H. Qiu, C. Qin, A. Schuh, K. Hammernik, and D. Rueckert. Learning diffeomorphic and modality-invariant registration using b-splines. In *Medical Imaging with Deep Learning*, 2021. URL `https://openreview.net/forum?id=eSI9Qh2DJhN`.

[37] H. Rahman, C.M. Scannell, O.M. Demir, M. Ryan, H. McConkey, H. Ellis, P.G. Masci, D. Perera, and A. Chiribiri. High-Resolution Cardiac Magnetic Resonance Imaging Techniques for the Identification of Coronary Microvascular Dysfunction. *JACC: Cardiovascular Imaging*, 14(5):978–986, 5 2021.

[38] H. Sakuma and M. Ishida. Advances in Myocardial Perfusion MR Imaging: Physiological Implications, the Importance of Quantitative Analysis, and Impact on Patient Care in Coronary Artery Disease. 21(1): 195–211, 2022.

[39] C.M. Scannell, A. Chiribiri, A.D.M. Villa, M. Breeuwer, and J. Lee. Hierarchical bayesian myocardial perfusion quantification. *Medical Image Analysis*, 60:101611, 2020.

[40] C.M. Scannell, E. Alskaf, N. Sharrack, R. Razavi, S. Ourselin, A.A. Young, S. Plein, and A. Chiribiri. AI-AIF: artificial intelligence-based arterial input function for quantitative stress perfusion cardiac magnetic resonance. *European Heart Journal - Digital Health*, 4(1):12–21, 1 2023.

[41] B. Sharif, R. Arsanjani, R. Dharmakumar, C.N. Bairey Merz, D.S. Berman, and D. Li. All-systolic non-ECG-gated myocardial perfusion MRI: Feasibility of multi-slice continuous first-pass imaging. *Magnetic Resonance in Medicine*, 74(6):1661–1674, 12 2015.

[42] M.J. Stewart. Contrast echocardiography. *Heart*, 89(3):342–348, 2003.

[43] R.A.P. Takx, B.A. Blomberg, H.E. Aidi, J. Habets, P. A. de Jong, E. Nagel, U. Hoffmann, and T. Leiner. Diagnostic accuracy of stress myocardial perfusion imaging compared to invasive coronary angiography with fractional flow reserve meta-analysis. *Circulation: Cardiovascular Imaging*, 8(1), 2014.

[44] Q. Tao, P. van der Tol, F. F. Berendsen, E.H.M. Paiman, H. J. Lamb, and R.J. van der Geest. Robust motion correction for myocardial T1 and extracellular volume mapping by principle component analysis-based groupwise image registration. *Journal of Magnetic Resonance Imaging*, 47(5):1397–1405, 5 2018.

[45] J. Tourais, C. Coletti, and S. Weingärtner. *Chapter 1 - Brief Introduction to MRI Physics*, volume 7 of *Advances in Magnetic Resonance Technology and Applications*. Academic Press, 2022.

[46] J. Tourais, C.M. Scannell, T. Schneider, E. Alskaf, R. Crawley, F. Bosio, J. Sanchez-Gonzalez, M. Doneva, C. Schülke, J. Meineke, J. Keupp, J. Smink, M. Breeuwer, A. Chiribiri, M. Henningsson, and T. Correia. Breathing Quantitative First-Pass Perfusion Cardiac MR Using Dual-Echo Dixon With Spatio-Temporal Acceleration. *Frontiers in Cardiovascular Medicine*, 9, 4 2022.

[47] J. Tsao, P. Boesiger, and K.P. Pruessmann. k-t BLAST and k-t SENSE: Dynamic MRI with high frame rate exploiting spatiotemporal correlations. *Magnetic Resonance in Medicine*, 50(5):1031–1042, 6 2003.

[48] T. Wech, K.P. Kunze, C. Rischpler, D. Stäb, P. Speier, H. Kostler, and S.G. Nekolla. A compressed sensing accelerated radial MS-CAIPIRINHA technique for extended anatomical coverage in myocardial perfusion studies on PET/MR systems. *Physical Medicine*, 64:157–165, 2019.

[49] S. Weingärtner. Medical imaging signals & systems, course slides MRI lecture 2, 2022.

[50] J. Xu, F. Cai, C. Geng, Z. Wang, and X. Tang. Diagnostic performance of CMR, SPECT, and PET imaging for the identification of coronary artery disease: A meta-analysis. *Frontiers in cardiovascular medicine*, 8, 2021.

[51] H. Xue, L.A.E. Brown, S. Nielles-Vallespin, S. Plein, and P. Kellman. Automatic in-line quantitative myocardial perfusion mapping: Processing algorithm and implementation. *Magnetic Resonance in Medicine*, 83(2):712–730, 2 2020.

[52] Y. Yang, C.H. Meyer, F.H. Epstein, C.M. Kramer, and M. Salerno. Whole-heart spiral simultaneous multi-slice first-pass myocardial perfusion imaging. *Magnetic Resonance in Medicine*, 81(2):852–862, 2 2019.

[53] Y. Zur, M. Wood, and L. Neuringer. Spoiling of transverse magnetization in steady-state sequences. *Magnetic Resonance in Medicine*, 21(2):251–263, 1991.